# Effective removal of arsenate from wastewater using aluminium enriched ferric oxide-hydroxide recovered from authentic acid mine drainage

K. L. Muedi[1]; H. G. Brink[1*]; V. Masindi[2]; J. P. Maree[3]

[1]Department of Chemical Engineering, Faculty of Engineering, Built Environment and Information Technology, University of Pretoria, Private Bag X20, Hatfield, 0028, South Africa, deon.brink@up.ac.za

[2]Department of Environmental Sciences, School of Agriculture and Environmental Sciences, University of South Africa (UNISA), P. O. Box 392, Florida, 1710, South Africa

[3]ROC Water Technologies, P O Box 70075, Die Wilgers, 0041, Pretoria, South Africa

## Highlights

- Successful synthesis of Fe/AlO(OH) from authentic acid mine drainage.
- High capacity adsorption of arsenate (102–129 mg/g) by synthesised Fe/AlO(OH).
- Arsenate adsorption insensitive to pH (2–10) and temperature (25–65 °C) variations.
- Physisorption/diffusion-controlled mechanisms dominated Arsenate adsorption.

## Graphical Abstract



-
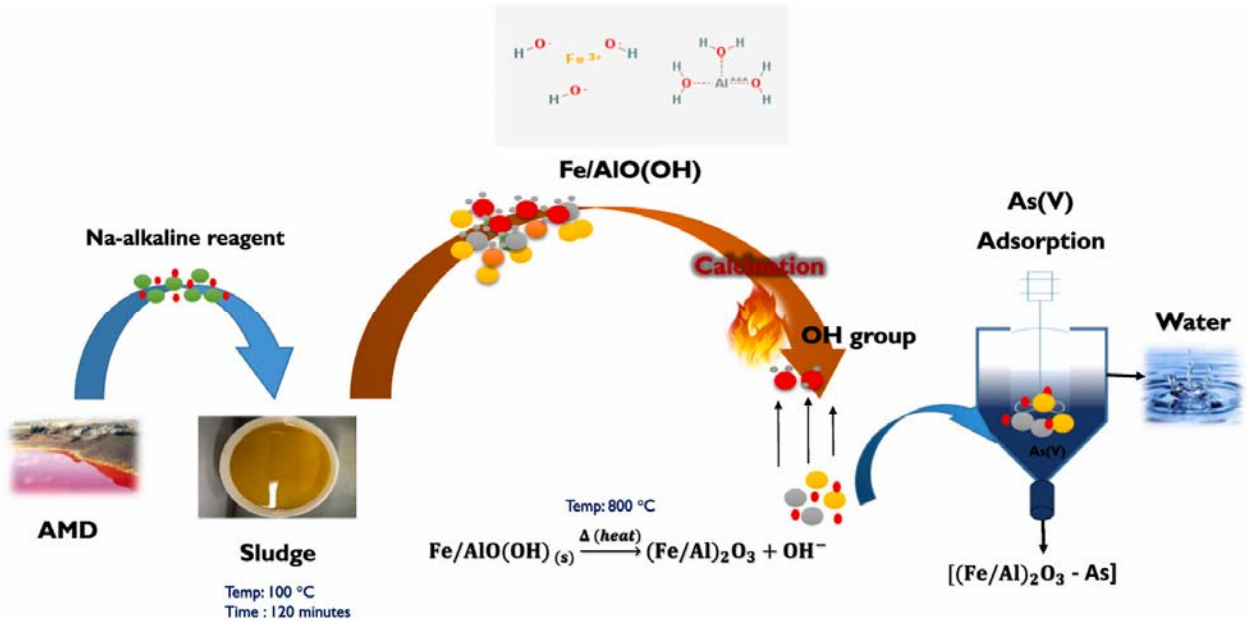
**Abstract**

This study explored an eco-friendly approach for the synthesis of novel aluminium enriched ferric oxide-hydroxide (Fe/AlO(OH)) from authentic acid mine drainage (AMD). The synthesized Fe/AlO(OH) was subsequently tested for arsenate removal capabilities. Fe/AlO(OH) was synthesized from *bona fide* AMD via selective precipitation, thermal activation, and vibratory ball milling. One-factor-at-a-time (OFAAT) method was used to optimize operational parameters, which include adsorbent dosage, concentration, pH, agitation time, and temperature. Optimized conditions were observed to be 150 ppm of As(V), Solid: Liquid ratio – 1g: 250 mL, contact time of 60 minutes, and ambient temperature and pH. Limited temperature and pH effects on adsorption were observed. Equilibrium data fits using Langmuir-, Freundlich-, Two surface Langmuir-, Dubinin-Radushkevich-, and Dubinin-Astokov isotherm models showed highly favorable adsorption conditions, the highest known maximum adsorption capacity for As(V) of 102 - 129 mg/g, and coupled physisorption/diffusion limited adsorption. Thermodynamic analysis showed positive Gibbs free energy ($\Delta G°$), negative enthalpy change ($\Delta H°$), and positive entropy change ($\Delta S°$) – likely a result of an inner sphere complexation of the As(V) with the Fe/Al surface. Considering the obtained results, valorization of AMD for the synthesis of Fe/AlO(OH) was viable and effective. This initiative could potentially minimize the footprints of AMD and arsenic pollution.

**Keywords:** Acid mine drainage; Arsenic; Adsorption; Aluminium; Ferric oxide-hydroxide

## 1. Introduction

Arsenic pollution continues to be a major global concern mostly due to the severity of its toxicity to living organisms upon exposure. Eco-toxicological and epidemiological studies have ranked arsenic amongst the top five (5) lethal contaminants threatening ecological systems and different environmental compartments [1]. Specifically, arsenic is discharged into the environment as part of industrial, mining, and metallurgical effluents, which ultimately cause detrimental impacts on the environment and human health. Arsenic pollution has led to its intake by plants and consumption by animals and humans, which also leads to bio-accumulation and bio-magnification in different trophic levels of the food chain [1]. Epidemiologically, arsenic can cause short and

2

long-term effects, such as diarrhoea, abdominal pain, cancer, and cardiovascular disease [2–4]. According to the World Health Organisation (WHO), the level of arsenic permitted in the environment ranges from 0.1 – 10 µg/L, which was set after several relevant toxicological studies [5]. The 10 µg/L limit also resulted from several studies which have been conducted on anthropogenic activities over the years, including water pollution by arsenic and other toxic chemical species [6]. The United States Environment Protection Agency (USEPA) presently uses the 10 µg/L arsenic standard which replaced the 50 µg/L to minimise health risks associated with arsenic exposure [7]. The South African National Standard (SANS) 241 has declared the allowable limit of arsenic concentration in drinking water to be $\leq$ 10 µg/L based on health impacts studies [8].

The prime toxic oxidation states of arsenic are arsenite [As(III)] and arsenate [As(V)], of which As(III) is the most toxic form and As(V) is the most mobile form. As(V) predominately exists as divalent ($HAsO_4^{2-}$) and monovalent ($H_2AsO_4^{-}$) species at near-neutral pH [9,10]. According to literature, arsenic levels in the environment can range between 0.01 – 700 ppm (10 µg/L – 700 000 µg/L) depending on the geographic regions, and can be present in air, water, soils, plants, the earth's crust, igneous and sedimentary rocks, animals, and humans [11,12]. A study by Hendricks et al. [13] reported the highest known arsenic concentration of 8000 ppm in an inorganic anionic state, detected in soils overlying deposits of sulphidic ore. The discharge of arsenic into water sources can originate from natural or anthropogenic activities. Primarily, natural sources of arsenic include weathering, erosion, geochemical reactions, and volcanic eruptions [11,12], whereas anthropogenic sources include agricultural activities, mining, smelting, burning of fossil fuels, wood preservation, and chemical weapon production [14]. The mobility of arsenic in surface and groundwater sources is accelerated by weathering and other leaching processes [11,12].

To abate and manage the challenges of arsenic in the environment several studies have explored methods for the removal of arsenic from water. These techniques include ion exchange [15], reverse osmosis [16], coagulation [17], precipitation [18], electro-sorption [19], and adsorption [20]. However, most of these technologies suffer from disadvantages including the generation of toxic sludge and high costs of operation and maintenance. Adsorption is considered a promising treatment technique for arsenic removal due to its low operational cost, high adsorbent regeneration capacity, low maintenance, and ease of operation. Various Fe and Al-based

3

adsorbents have been used for the removal of arsenic from water, including aluminium hydroxide [21], FeOOH/γ-Al$_2$O$_3$ granules [9] , magnetite-maghemite nanoparticles [22], and goethite [10].

Acid mine drainage (AMD) is usually an undesirable by-product of coal and gold mining activities, and results from hydro-geochemical weathering of sulphide-bearing minerals such as pyrite. AMD tends to be grossly enriched with aluminium (Al), iron (Fe), sulphate (SO$_4^{2-}$), and traces of other contaminants. In light of its chemical composition, AMD could be considered as a viable source of Al, Fe, and SO$_4^{2-}$ for beneficiation and valorisation. Traditionally, iron and aluminium oxides have been synthesised from synthetic chemicals. Pehlivan et al. [23] used synthetic aluminium nitrate nonahydrate and iron nitrate nonahydrate to synthesise Al$_2$O$_3$ and Fe$_2$O$_3$ through solution combustion. Braga et al. [24] synthesised aluminium oxide/iron oxide by mixing chitosan and iron and aluminium hydroxides through dissolution and continuous stirring. Hübner et al. [25] synthesised aluminium/iron oxide/hydroxide nanothermite compounds via co-precipitation of synthetic iron (III) chloride hexahydrate in the presence of spherical aluminium nanoparticles (Al/Al$_2$O$_3$).

Recently, a notable number of studies have reported the recovery of Al, Fe, and SO$_4^{2-}$ from AMD while exploring potential applications. Akinwekomi et al. [26] evaluated the recovery of Fe(II) and Fe(III) from AMD and evaluated its utilisation in the synthesis of magnetite. Furthermore, similar authors explored the synthesis of goethite, hematite, magnetite, and gypsum from AMD [27]. The primary aim was to foster the circular economy and minimize ecological impacts of acid mine drainage. Ryan et al. [28] studied the precipitation of iron oxide pigments from synthetic AMD. Masindi et al. [29] studied and reported the efficiency of cryptocrystalline magnesite on the recovery of metals from AMD, including Fe, Al, Zn, and gypsum. Seo et al. [30] reported on the successful recovery of Fe, Al, and Mn from coal AMD via selective precipitation. These studies have proven that Fe and Al can be recovered in significant quantities from AMD. Specifically, Fe and SO$_4^{2-}$ are of viable quantities ranging to 6000 and 80000, respectively [27,31] whilst the remaining contaminants are prevalently below 200 ppm [32]. Generally, different alkaline agents are used to recover minerals from AMD including limestone, lime, hydrated lime, magnesite, calcined magnesite, brucite, periclase, soda ash, caustic soda, and alkaline-based-tailings [33].

Considering the two toxic and hazardous streams, arsenic effluents and AMD, an elegant solution lies in the recovery of Fe and Al from authentic AMD via fractional and step-wise precipitation

4

and subsequent use of the precipitate as an adsorbent for the removal of arsenic from water. This would simultaneously ameliorate the detrimental impact of both AMD and arsenic in the environment hence fostering the concept of circular economy and mineral valorisation. Consequently, this study aimed to recover Al/Fe poly-cations by fractional precipitation of authentic AMD and subsequently exploring the application of the precipitate in the removal of arsenic from simulated wastewater.

## 2.    Materials and methods

### 2.1    Feedstock and samples collection

Acid mine drainage (AMD) was collected from a coal mine in Mpumalanga Province, South Africa. Caustic soda (NaOH) which was used for pH control and AMD neutralisation was purchased from Merck (Pty) Ltd. (Johannesburg, South Africa). Sodium arsenate dibasic heptahydrate was purchased from Fluka Analytical (Munich, Germany). All chemicals were of analytical grade. Reaction vessels (glassware) were thoroughly cleaned with deionized water before every use, and all solutions were prepared using ultrapure water (18.2 MΩ-cm).

### 2.2    Synthesis of Aluminium enriched Ferric oxide-hydroxide (Fe/AlO(OH)) from AMD

Fe/AlO(OH) was synthesised through selective precipitation. Sodium hydroxide provides $OH^-$ ions which react with $Fe^{3+}/Al^{3+}$ to form insoluble $Fe/Al(OH)_3$. According to literature $Fe(OH)_3$ and $Al(OH)_3$ precipitates at pH > 2 [26]. Findings from a previous research study [31] revealed a pH of 4.5 as adequate in the simultaneous recovery of Al and Fe from authentic AMD. A known volume of AMD was dosed with dry NaOH to increase the solution pH from 2.5 to 4.5 for selective precipitation. The mixture was subsequently mixed for 60 minutes using an overhead stirrer at room temperature (±24 ºC). The resultant mixture was slowly heated to 100 °C while continuously stirring. After heating, the flask was left to cool to room temperature, vacuum filtered using Whatman® Grade 40 ash-less filter paper and dried at room temperature. Post drying, the recovered and synthesized Fe/AlO(OH) samples were vibratory-ball-milled to a fine powder at a speed of 700 rpm. Subsequently, the material was calcined at 800 °C and then sieved through a 32 μm perforated sieve to acquire the desired particles. The samples were stored in a plastic "zip-lock" bag, to protect against the elements, until used for arsenic removal.

## 2.3    Preparation of arsenate stock solution

The As(V) stock solution with 1000 mg.L$^{-1}$ of As(V) was prepared by dissolving 4.1646 g of Sodium arsenate dibasic heptahydrate (Na$_2$HAsO$_4$.7H$_2$O) salt in ultrapure water (18.2 MΩ-cm). The stock solution was prepared in 1000 mL volumetric flask. Fresh working solutions of As(V) were prepared for each experiment.

## 2.4    Batch experiments

All adsorption kinetic experiments were conducted on magnetic stirrers, and isotherm experiments in a thermal orbital shaker/incubator, containing 250 mL As(V) solutions in 250 mL Erlenmeyer flasks, mixed at an agitation speed of 250 rpm. Batch-scale experiments for the adsorption of As(V) (adsorbate) by Fe/AlO(OH) (adsorbent) were conducted to evaluate the effects of initial As(V) concentration, initial pH of As(V) solution, the dosage of the adsorbent, agitation time and temperature. All the experiments were carried out in triplicates and the mean value reported. According to Frey et al. [34] parameter design, i.e. the choice of nominal operational values for a set of design parameters, is preceded firstly by concept design (the set of design parameters) and then tolerance design (the allowable range for the operational parameters). Due to the exploratory nature of this study, with regards to the adsorption of As(V) on the synthesised material, the exact operational parameters as well as the satisfactory range for these parameters were still unknown. Consequently, a one-factor-at-a-time experimental procedure was chosen to give insight into the magnitude of influence the parameters have on adsorption as well as the feasible range of the parameters that yield satisfactory adsorption. A summary of the studied experimental parameters is shown in Table 1.

**Table 1: Summary of studied parameters for As(V) adsorption**

| Experiment | Initial As(V) concentration (mg.L$^{-1}$) | Adsorbent Dosage (g) | Experimental time (min) | Initial pH of As(V) solution | Temperature (°C) |
|---|---|---|---|---|---|
| 1 | 1; 5; 10; 20; 30; 40; 50; 100; 150; 200; 250; 300; 350; 400 | 1 | 90 | 7 − 8 | 25 |
| 2 | 150 | 0.1; 0.5; 1; 2; 3; 4; 5 (±0.0005) | 90 | 7 − 8 | 25 |
| 3 | 150 | 1 | 10; 30; 60; 90; 120; 180; 240; 300 | 7 − 8 | 25 |
| 4 | 150 | 1 | 90 | 2, 3, 4, 5, 6, 7, 8, 9, 10 (±0.2) | 25 |
| 5 | 150 | 1 | 90 | 7 − 8 | 25; 35; 45; 55; 65 |

To study the effects of initial As(V) concentration on the adsorption study, fresh aqueous solutions were prepared from the concentrated (1000 mg.L$^{-1}$) As(V) stock solution. The effects of Fe/AlO(OH) dosage on the removal of arsenic from aqueous solution was evaluated by weighing masses of the adsorbent on a 4-decimal point mass balance and add them in their respective flasks. In studying the effect of agitation time, batch sets were run for different mixing time intervals. For the determination of the effect of initial pH of As(V) solution, 0.1 M NaOH and/or 0.1 HNO$_3$ were used to adjust the pH to a desirable level. The effect of temperature was determined by conducting the adsorption experiments in a thermal orbital shaker/incubator at fixed temperature, shaking speed, and time. Blank and zero samples were also analysed to verify the concentration and compare analytical results to the theoretical concentrations.

Isotherm experiments were performed by running batch experiments containing 1 g adsorbent suspended in 250 mL Erlenmeyer flasks containing 250 mL As(V) solutions. The experimental conditions used for the isotherm experiments are reported in Table 2.

**Table 2: Summary of studied parameters for As(V) adsorption isotherms**

| Experiment | Initial As(V) concentration (mg.L$^{-1}$) | Adsorbent Dosage (g) | Experimental time (hours) | Initial pH of As(V) solution | Temperature (ºC) |
|---|---|---|---|---|---|
| 1 | 200; 250; 300; 350; 400 | 1 | 24 | $7 - 8$ | 25 |
| 2 | 200; 250; 300; 350; 400 | 1 | 24 | $7 - 8$ | 35 |
| 3 | 200; 250; 300; 350; 400 | 1 | 24 | $7 - 8$ | 45 |

## 2.5 Characterization of aqueous samples

The pH levels of aqueous solutions before and after chemical reactions were determined using a Thermo Scientific™ Orion 3 Star portable pH meter. Electrical conductivity (EC), total dissolved solids (TDS), and salinity were determined using a Mettler Toledo (Columbus, OH (USA)) FiveGo EC/TDS/Salinity/Temperature portable multimeter. The aqueous concentrations of chemical species were analysed using ICP-MS (7500ce, Agilent, Alpharetta, GA, USA). The pH, EC, TDS, salinity, and chemical composition of the raw AMD are reported in Supplementary Table 1 and shows that the AMD is an excellent source of Al ($280 \pm 2$ mg.L$^{-1}$), Fe ($1818 \pm 4$ mg.L$^{-1}$) and SO$_4^{2-}$ ($80000 \pm 10$ mg.L$^{-1}$).

## 2.6 Characterization of solid samples

The mineralogical composition and pattern of Fe/AlO(OH) and the residue products were determined using X-ray diffraction (XRD) and recorded on a Panalytical X'Pert PRO equipped with Cu-Kα radiation. X-ray fluorescence (XRF) (Thermo Fisher ARL-9400 XP+ Sequential XRF with WinXRF software) was used to determine the compound composition of the Fe/AlO(OH). The XRF analysis of the synthesised Fe/AlO(OH) is reported in Supplementary Table 2. Surface morphology and composition of the solid samples were characterized using high-resolution scanning electron micrographs (HR-SEM-EDS) (Model: Sigma VP FE-SEM with Oxford EDS Sputtering System, Make: Carl Zeiss, Supplier: Carl Zeiss, USA). The metal functional groups in the solid samples were analysed by using a Perkin-Elmer Spectrum 100 Fourier Transform Infrared

Spectrometer (FTIR) equipped with a Perkin-Elmer Precisely Universal Attenuated Total Reflectance (ATR) sampler. BET surface area and BJH pore size of the Fe/AlO(OH) and resultant residues were determined using a Brunauer-Emmet-Teller (BET) equipment equipped with Micromeritics VacPrep 061 degassing system (Micromeritics Tri-Star II 3020, Surface area and porosity, Poretech CC, USA). The thermal stabilities of Fe/AlO(OH) and residue products were detected using a Thermo Gravimetric Analyser (TGA) (TGA Q500, TA instrument) under atmospheric air with a flow rate of 50 mL.min$^{-1}$ and a heating rate of 10˚C.min$^{-1}$.

## 2.7    Point of zero charge (PZC)

In studying and determining the point of zero charge (PZC) of the adsorbent (Fe/AlO(OH)), a method described by Smičiklas et al. [35] was adopted and applied. A volume of 50 mL of 0.1 M KNO$_3$ solution was transferred into nine (9) individual flasks. The initial pH values of the solutions were adjusted to 2 – 10 using 0.1 M HNO$_3$ and NaOH. Thereafter, 0.1 g of Fe/AlO(OH) was added into each flask and the mixtures were left allowed to equilibrate for 24 hours at ± 25 ºC. The Fe/AlO(OH) suspensions were then separated from the solutions, and the final pH values were recorded.

## 2.8    Adsorption capacity and removal efficiency

### 2.8.1 Adsorption capacity

The adsorption capacity of Fe/AlO(OH) and percentage removal of As(V) from aqueous solution was determined using equation 1 [36]:

$$Q_e = \frac{(C_0 - C_e).V}{m} \tag{1}$$

Where, $Qe$ (mg.g$^{-1}$) is the adsorption capacity; $C_o$ (mg.L$^{-1}$) is the initial concentration of As(V), $Ce$ (mg.L$^{-1}$) is the equilibrium concentration of As(V), respectively; $V$ (L) is the volume of the As(V) solution; and $m$ (g) is the dosage of the adsorbent.

### 2.8.2    Percentage removal

The adsorption capacity of Fe/AlO(OH) and removal efficiency of As(V) with the adsorbent from aqueous solution was determined using equation 2:

$$\%R_e = \frac{C_0 - C_e}{C_0} \times 100 \tag{2}$$

Where; $\%R_e$ is the removal efficiency of the adsorbent; $C_0$ is the initial As(V) concentration (mg/L); $C_e$ is the equilibrium As(V) concentration (mg.L$^{-1}$).

## 2.9    Desorption study

To study the regeneration of the Fe/AlO(OH), a method described by Kumari et al. [37] was applied. A batch experiment was conducted where 1 g of Fe/AlO(OH) was agitated with 250 mL of 150 mg.L$^{-1}$ As(V) solution in a 250 mL Erlenmeyer flask for 90 minutes. After equilibration, the residue was separated from the supernatant via centrifugation. The recovered residue material was then washed five times with 250 mL ultra-pure water to remove excess As(V) ions, and then dried. Thereafter, the dried sample was mixed with 250 mL of 0.1 M HNO$_3$ under room temperature. The resultant HNO$_3$ extract was collected and analysed for As(V) ions. The desorption percentage was determined using Equation 3:

$$\%Desorption = \frac{C_{des}}{C_o} \times 100 \tag{3}$$

Where; $C_{des}$ (mg.L$^{-1}$) is the concentration of As(V) ions in the desorption eluent; $C_o$ (mg.L$^{-1}$) is the initial concentration of As(V) ions.

## 3.    Results and discussion

### 3.1    Characterisation of Raw Fe/AlO(OH) (RP) and Post As-adsorption (PA) Fe/AlO(OH)

#### 3.1.1 Functional groups on surfaces

Figure 1 depicts the functional groups present in the material before and after As(V) adsorption after characterisation with FTIR.
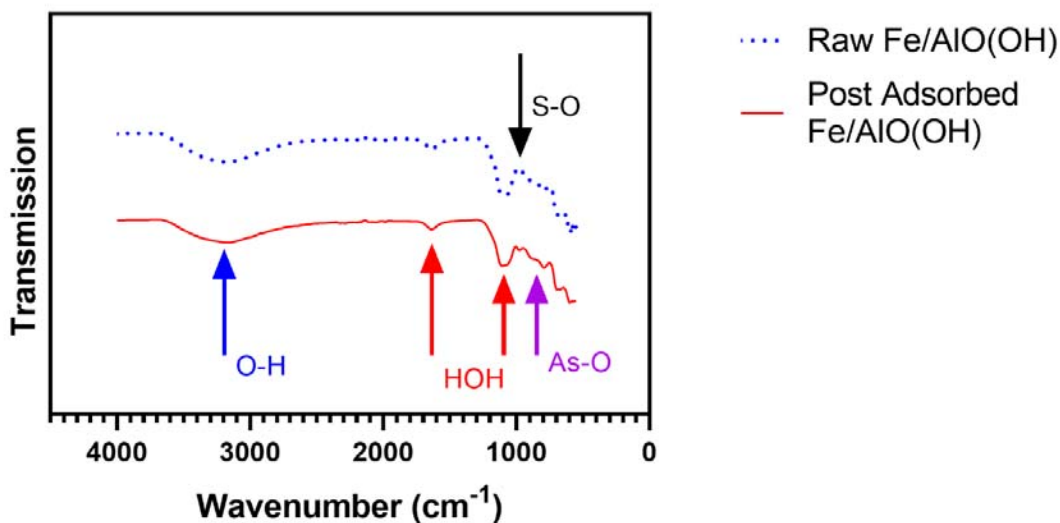
**Figure 1: Functional groups of raw and As(V)-reacted Fe/AlO(OH)**

Bands of raw and As(V)-reacted Fe/AlO(OH) are shown in Figure 1. An illustration of possible high stretching of O−H for the two parallel bands is observed between 4000 –3500 $cm^{-1}$. The adsorption band at 1668 $cm^{-1}$ could be an indication of the stretching of HOH which further increased at 1113 $cm^{-1}$ [38]. The broad band around 1100 $cm^{-1}$ indicate surface bound S–O groups [39]. The small band at 839 $cm^{-1}$ which curves upwards could be an indication of the stretching of As−O [38].

### 3.1.2 Surface morphology

Figure 2 illustrates the distribution of morphology in Fe/AlO(OH) determined using SEM before (RP) and after As(V) adsorption (PA). There is no significant change in the morphology of the material before and after contacting As(V). Figure 2(a), (c), and (e) show the morphologies of the raw Fe/AlO(OH)  at different sizes. The Fe/AlO(OH) shows non-uniform shapes with uneven distribution of irregular agglomerates.  The material is observed to have pressed-like structures. When compared to the morphologies of As-reacted Fe/AlO(OH) depicted in Figure 2(b), (d) and (f), there is no significant difference due to the material's high stability. This indicates that the synthesized Fe/AlO(OH) is chemically and mechanically stable. Similarly, Jiménez-Cedillo et al. [40] and Nekhunguni et al. [9] reported that no clear change was observed after adsorption using their studies' pollutants.
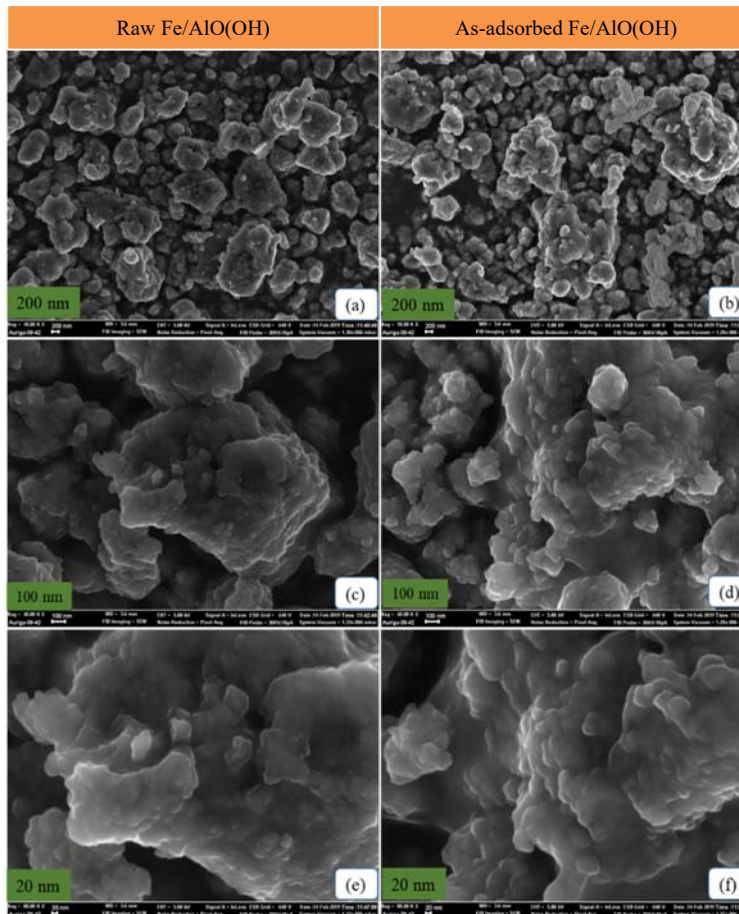
11

**Figure 2: Morphology of Fe/AlO(OH) before (a, c, and e) and after (b, d, and f) As(V) adsorption**

### 3.1.3 Mineral composition

Figure 3 illustrates the mineral composition of the Fe/AlO(OH) before and after As(V) adsorption, respectively, after characterisation with XRD.  Figure 3 illustrates that the synthesized Fe/AlO(OH) was amorphous in nature. This could be explained by the deficiency of peaks within the diffractogram. Furthermore, the Fe/AlO(OH) was principally characterised by goethite FeO(OH) as the main mineral and crystalline phase. As such, it can be concluded that the adsorption of As(V) did not impact the mineralogical composition of the synthesized Fe/AlO(OH), thereby possibly showing the adsorption of As on the surface of the material without altering its crystalline structure [41], albeit with a highly amorphous nature.  This further confirms that the material is chemically stable.
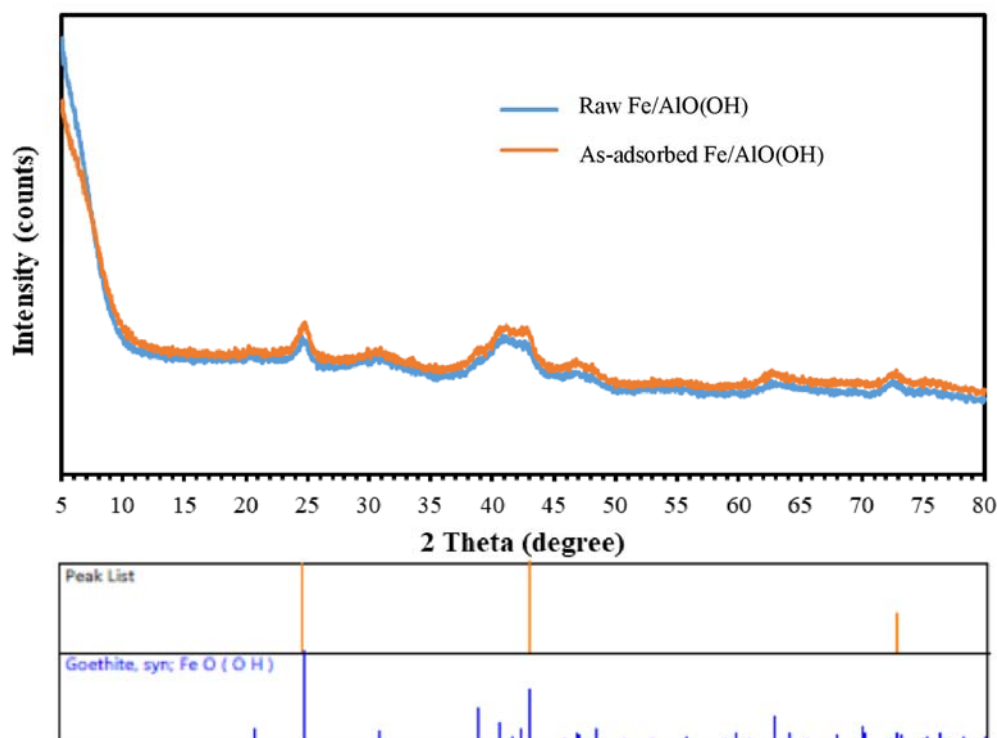
12

**Figure 3: The XRD diffractogram of raw and As adsorbed Fe/AlO(OH).**

### 3.1.4 EDS analysis and corresponding mapping of elemental composition

The results from EDS spectral elemental analyses of the adsorbent surface of the raw and As reacted Fe/AlO(OH) are shown in Figure 4. The relative compositions were determined by taking the means of four spot-spectra on the Fe/AlO(OH). All spectra show the presence of Fe and Al thereby confirming the metallic nature of the material. The presence of Fe and S denotes that this material was recovered from pyritic AMD. The significant presence of oxygen represents the oxide fraction of the adsorbent. The presence of Si, S, Mg, Ca and other minor component are the result of impurities co-precipitated from the AMD. The presence of As on the surface after adsorption indicates that the material scavenges arsenic from aqueous solution and thereby confirms the fate of the adsorbed species. Moreover, the composition of Fe, Al, S, O and C was observed to be preserved during adsorption therefore demonstrating the chemically stability of the material – a Student's t-test showed insignificant differences (5% level) in the means of all respective elements present before and after adsorption. The XRF chemical composition of the Fe/AlO(OH)

13

(Supplementary Table 2) support these result as a majority of $Fe_2O_3$ and $Al_2O_3$, with minor components Si, S, Mg, Ca, etc, were measured in the solid matrix prior to adsorption.
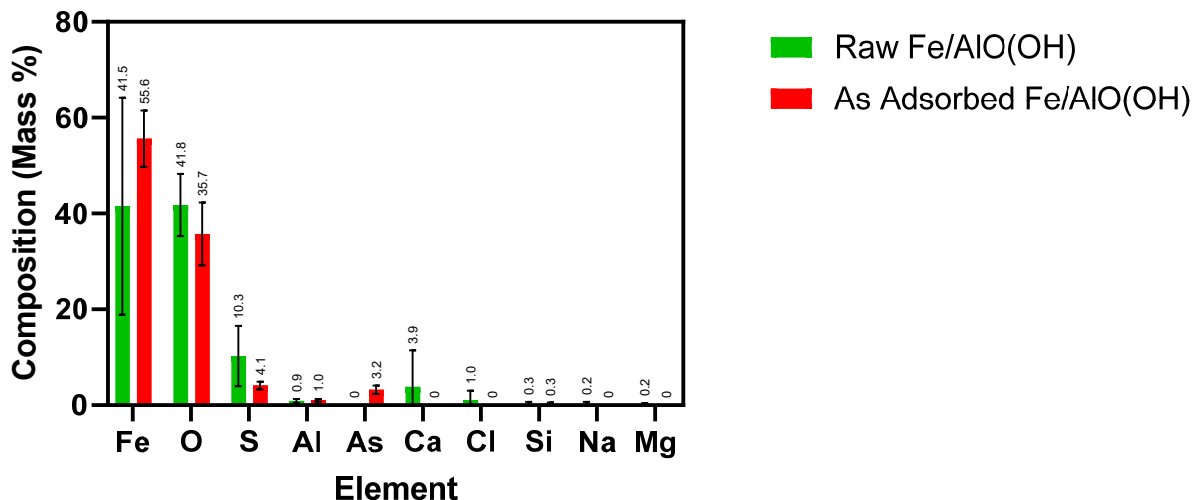


**Figure 4: Comparison of EDS elemental analyses of raw Fe/AlO(OH) and As adsorbed Fe/AlO(OH)**

The EDS mapping of the relative distribution of elements on the raw (RP) and As adsorbed (PA) surfaces of Fe/AlO(OH) are shown in Figure 5. Figure 5 shows that Fe and Al are present in the synthesised Fe/AlO(OH) in a uniform and even distribution. The presence of O likely shows the oxide part of the adsorbent. From the main structure (a), appearances of Fe and Al are observed. As was detected on the PA mapped surfaces confirming the fate of As(V) after adsorption by the Fe/AlO(OH).

From the corresponding maps for the individual species measured by the EDS, as shown in Figure 5, similar distribution patterns for the individual species can be observed. This observation might indicate that different elements were present within the same area on the surface, likely as a result of the precipitating species identities (e.g. O and Fe/Al as in $Fe_2O_3$, $Al_2O_3$), possible co-precipitation (Fe and S), or the interaction of the As species with the surface species.
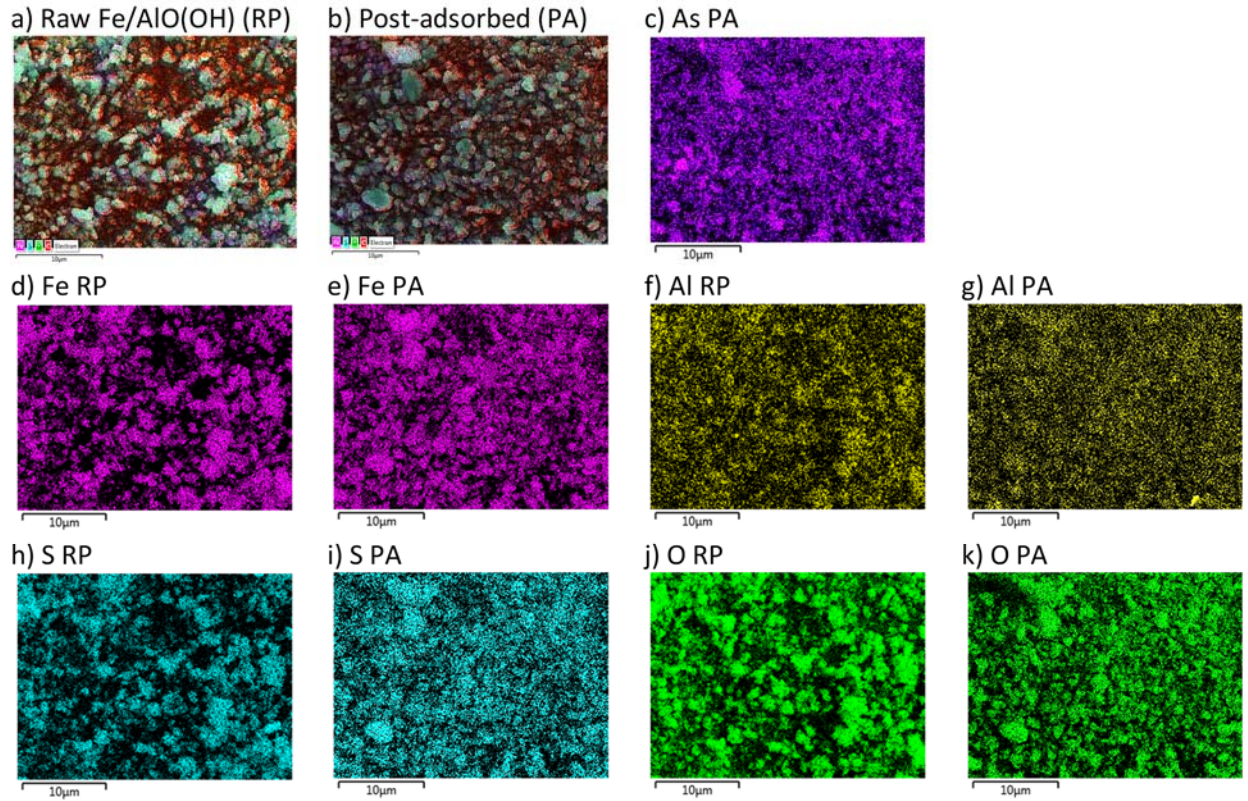
14

**Figure 5: EDS mapping of the Raw Fe/AlO(OH) (RP) and Post As(V)-adsorbed (PA) Fe/AlO(OH) . The maps show the elemental distribution of all elements (a and b), As (c), Fe (d and e), Al (f and g), S (h and i), and O (j and k).**

To quantitatively assess the interaction of the species, the images in Figure 5 were compared using image processing software ImageDiff. The process involves a modification of the Recursive Pixel Allocation method [42] and involves the comparison of corresponding pixels in associated images to assess the prevalence of co-occupation of various elemental species in the pixels. To ensure comparable images, the images were cropped to a constant size of 200×270 pixels (surface are of 765.3 $\mu m^2$), to remove all white borders – which would yield a false positive area. The cropped areas were the same distance from the top of the image (26 pixels) and the left of the image (6 pixels) to ensure that compared areas corresponded to the same zones from the original image. To account for the differences in colour between the images, each image was first normalised against a pure black image – the EDS represented the absence of species as black – using a high and low threshold filter and the resulting images were converted to monochrome. The high threshold filter ignored all pixels except those with the maximum difference compared to the black image and *vice versa* and therefore provided a method to assess the extreme differences between black image and

15

the image of interest. The resulting monochrome images were subsequently compared on a pixel level. The interaction matrices between the measured species are shown in Table 3 and Table 4.

**Table 3: The interaction matrix showing the average ± standard deviations of the percentage differences between corresponding pixels for the raw Fe/AlO(OH)**

|       | Fe RP          | Al RP          | S RP           | O RP           |
|-------|----------------|----------------|----------------|----------------|
| Fe RP | 0 %            | 46.4 ± 7.5 %   | 37.0 ± 4.4 %   | 35.7 ± 4.0 %   |
| Al RP | 46.4 ± 7.5 %   | 0.0 %          | 41.9 ± 7.6 %   | 35.4 ± 6.5 %   |
| S RP  | 37.0 ± 4.4 %   | 41.9 ± 7.6 %   | 0.0 %          | 30.1 ± 3.0 %   |
| O RP  | 35.7 ± 4.0 %   | 35.4 ± 6.5 %   | 30.1 ± 3.0 %   | 0.0 %          |

**Table 4: The interaction matrix showing the average ± standard deviations of the percentage differences between corresponding pixels for the post As(V)-adsorbed (PA) Fe/AlO(OH)**

|       | Fe PA          | Al PA          | S PA           | O PA           | As PA          |
|-------|----------------|----------------|----------------|----------------|----------------|
| Fe PA | 0 %            | 49.4 ± 2.7 %   | 46.0 ± 0.9 %   | 43.4 ± 1.4 %   | 49.2 ± 2.4 %   |
| Al PA | 49.4 ± 2.7 %   | 0.0 %          | 50.7 ± 3.4 %   | 24.5 ± 4.8 %   | 26.1 ± 7.9 %   |
| S PA  | 46.0 ± 0.9 %   | 50.7 ± 3.4 %   | 0.0 %          | 45.8 ± 0.5 %   | 50.1 ± 3.1 %   |
| O PA  | 43.4 ± 1.4 %   | 24.5 ± 4.8 %   | 45.8 ± 0.5 %   | 0.0 %          | 18.8 ± 4.1 %   |
| As PA | 49.2 ± 2.4 %   | 26.1 ± 7.9 %   | 50.1 ± 3.1 %   | 18.8 ± 4.1 %   | 0.0 %          |

The data presented in Table 3 and Table 4 were validated by a Student's t-test of the corresponding interactions for the tables. E.g. the t-test probability of a significant difference between the means of Fe RP – Al RP and Fe PA – Al PA was 0.66, well above the generally accepted significance level of 0.05. This shows that an insignificant difference between the means of the compared interaction pairs existed. None of the t-tests showed significant differences in means at a significance level of 5% and therefore it was assumed that Table 3 and Table 4 represented the properties for comparable materials.

From Table 3 and Table 4, it can be observed that the smallest differences in surface occupation were observed in the As−Al, As−O, Al−O, and S−O species. The As−Al interaction shows a disproportionate Al effect on As(V) adsorption considering the circa 1% prevalence of Al in the adsorbent (Figure 4 and Supplementary Table 2); likely a result of the large charge differences in

16

the species. This interaction has been reported previously in literature [43–45]. The As−O interaction likely resulted from the As oxyanion species, the S−O species were likely a result of the significant sulfate content of the AMD used for synthesis. Both As−O and S−O species were observed in the FTIR spectrum (Figure 1). The Al−O interactions were likely a result of the precipitation of $Al_2O_3$ species. The relatively high prevalence of Fe−O surface occupation links to the oxygenated goethite species observed in the XRD spectrum (Figure 3). It is interesting to observe the prevalence of Fe−S co-occupation which can be ascribed to sulfate-geothite surface bonding as observed by Peak et al. [39].

### 3.1.5 Thermal stability

Figure 6 illustrates the thermal stability of Fe/AlO(OH) before and after As(V) adsorption, as analysed using thermos-gravimetric analysis.
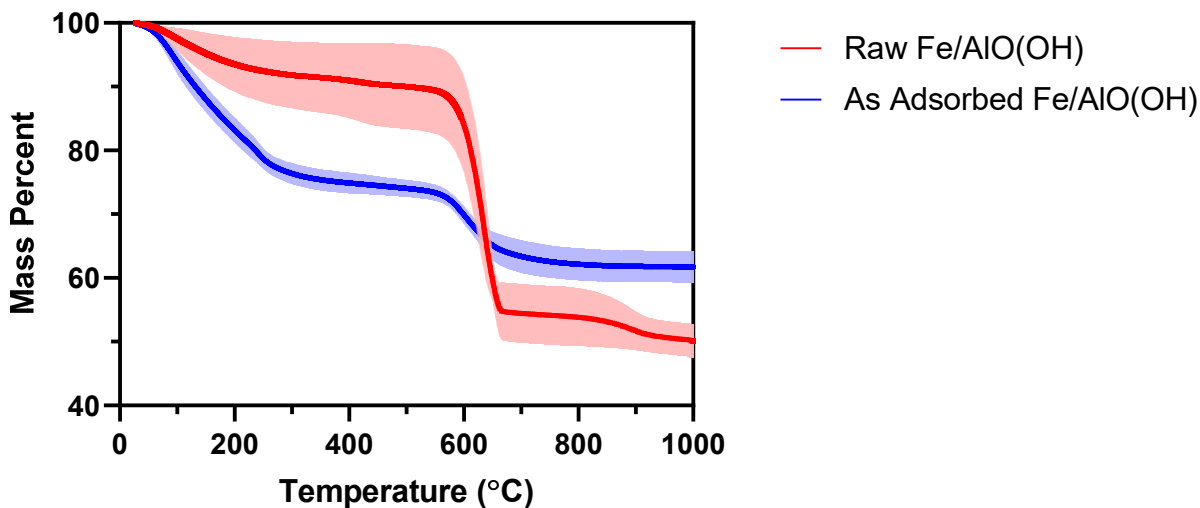


**Figure 6: Thermal stability of Fe/AlO(OH) before and after As(V) adsorption. The shaded areas show the standard deviations of four repeat measurements.**

Figure 6 demonstrates the thermal stability of Raw (RP) and Post As-adsorbed (PA) Fe/AlO(OH). Longa-Avello [46] reported a three-stage calcination process for Goethite, the first stage at temperatures between 250 °C – 350 °C involves the moisture loss from the mineral. The second stage (450 °C – 550 °C) involves the loss of chemically bound water, and the final stage above 550 °C involves the loss of OH⁻-groups. These stages of calcination were clearly observed in the TGA graph for both RP and PA Fe/AlO(OH) (Figure 6). Regarding the influence of the inclusion

17

of Al within the mineral matrix, Wei et al. [47], in a study which evaluated the thermal stability of an atomically sharp Fe/Al interface, also reported a temperature of 150 ºC as being the maximum temperature before the state of Fe/Al interface could change as further heating changes the chemical structure of the material.  It should be noted that significant differences were observed between thermal stabilities of RP and PA Fe/AlO(OH). It is observed that the first stage in the PA was significantly more pronounced than the RP, the second stage was very similar for both RP and PA, while the As(V) adsorption appeared to stabilise the adsorbent material. A likely explanation for the different TGA profiles for the RP and PA Fe/AlO(OH) is that the adsorption of As(V) disrupts $OH^-$ groups as a result of the inner sphere complexation which displaces of $H_2O/H^+$ during adsorption [48]; this significantly reduces the release of $OH^-$-groups at temperatures above 550 °C.

### 3.1.6 Surface area and porosity of Fe/AlO(OH) pre- and post As-adsorption

The surface area properties of the raw Fe/AlO(OH) (RP) and As-adsorbed (PA) Fe/AlO(OH) are shown in Table 5. The surface properties were calculated using the methods of Brunauer, Emmett and Teller (BET), and Barrett, Joyner and Halenda (BJH) to determine the specific surface area and the pore size distribution of the porous material, respectively [49]. The large differences in the adsorption average pore width and the BJH average pore diameter (see Table 5) result from the assumptions that these methods are based on. The adsorption average pore width assumes the presence of uniform cylindrical pores (calculated as the ratio of adsorption total pore volume and BET surface area), while the BJH average pore diameter is calculated using the assumptions that the pores contain a surface on which layers of adsorbate molecules can form which increase proportional to the relative pressure of adsorbate, and there exists a capillary radius which is filled by adsorbate condensate. The BJH method calculates the average pore diameter taking into account the adsorbed layer and the capillary condensed adsorbate [49]. The adsorption total pore volume was calculated from the volume of nitrogen adsorbed at saturation conditions by assuming the adsorbed nitrogen has the same density as the liquid phase at the operational temperature. In contrast, the BJH cumulative volume is calculated from the incremental sum of the pore volumes, considering the pore size distribution effect and the relative contributions of adsorbate adsorption and condensation on the total amount of adsorbate retained in the adsorbent [49].

18

**Table 5: The surface area properties of the Raw Fe/AlO(OH) and As-adsorbed Fe/AlO(OH)**

| Parameters | | |
|---|---|---|
| Surface Area (m².g⁻¹) | Raw Fe/AlO(OH) | As-adsorbed Fe/AlO(OH) |
| BET Surface Area | 37.6 | 82.0 |
| Pore Volume (cm³.g⁻¹) | | |
| Adsorption total pore volume | 0.0621 | 0.0902 |
| BJH cumulative volume | 0.0630 | 0.0762 |
| Pore Size (nm) | | |
| Adsorption average pore width | 6.60 | 4.40 |
| BJH average pore diameter | 22.7 | 14.2 |

As shown in Table 5, the BET surface area of the Fe/AlO(OH) was reported to be approximately 37.6 m².g$^{-1}$ which significantly increased to approximately 82.0 m².g$^{-1}$ after the adsorption of As(V) ions from aqueous solution. An increase in surface area indicates that the adsorbed chemical has the potential to increase the surface area of the adsorbent which indicates the potential of this material for secondary uses post the adsorption of As(V) ions. In addition, the adsorption total pore volume and the BJH cumulative volumes increased markedly when comparing the pre- and post As(V)-adsorbed Fe/AlO(OH). The increased total pore volume might indicate the "hollowing out" of the particle itself during adsorption. This was possibly a result of the release of bound water and protons due to inner sphere complexation [48] or the initial oxyanion assistant dissolution of the goethite at low surface coverage due to mononuclear inner sphere complexation (the material was later stabilized at higher surface coverage due to binuclear inner sphere complexation) [50], but the exact mechanism responsible is yet to be determined. This "hollowing" of the adsorbent further provides a likely explanation for significant increase in BET surface area even though the pore diameters decrease during adsorption.

The raw Fe/AlO(OH) and As-adsorbed had BJH pore sizes of 22.7 nm and 14.2 nm, which denotes that the material is mesoporous – the pore diameter falls within the range of 2 – 50 nm [51]. Some studies have reported low surface areas of mesoporous materials for $Fe_2O_3$ and $Al_2O_3$ to be 5.05 and 0.50 m².g$^{-1}$, and 0.55 and 2.35 m².g$^{-1}$, respectively [43,52], while other studies reported high surface areas of Fe-Al materials of 47 – 134 m$^2$/g [53,54].

The nitrogen adsorption-desorption isotherms of the synthesized Fe/AlO(OH) and As-reacted Fe/AlO(OH) are shown in Figure 7. The adsorbed quantities were observed to increase with an

increase in relative pressure. This could be explained by the non-rigid nature of the adsorbent and the location of the characteristic shoulder is consistent with the destabilization of condensate at the $P/P^0$ value, which is limiting the entire process. Furthermore, the curve for the raw Fe/AlO(OH) and As-adsorbed Fe/AlO(OH) showed type IV adsorption isotherm behavior. Moreover, Figure 7 showed H3-type hysteresis loops according to BDDT classification, indicating the samples contain meso-pores (2–50 nm) and will therefore enable high permeability of the contaminated water hence increasing the rate at which contaminants are scavenged out of the solution [51,55,56]. The nitrogen adsorption-desorption curve closely resembles that reported by Zhang et al [56] which was also interpreted as conforming to H3-type hysteresis with similar surface area and pore size as that measured in this study.
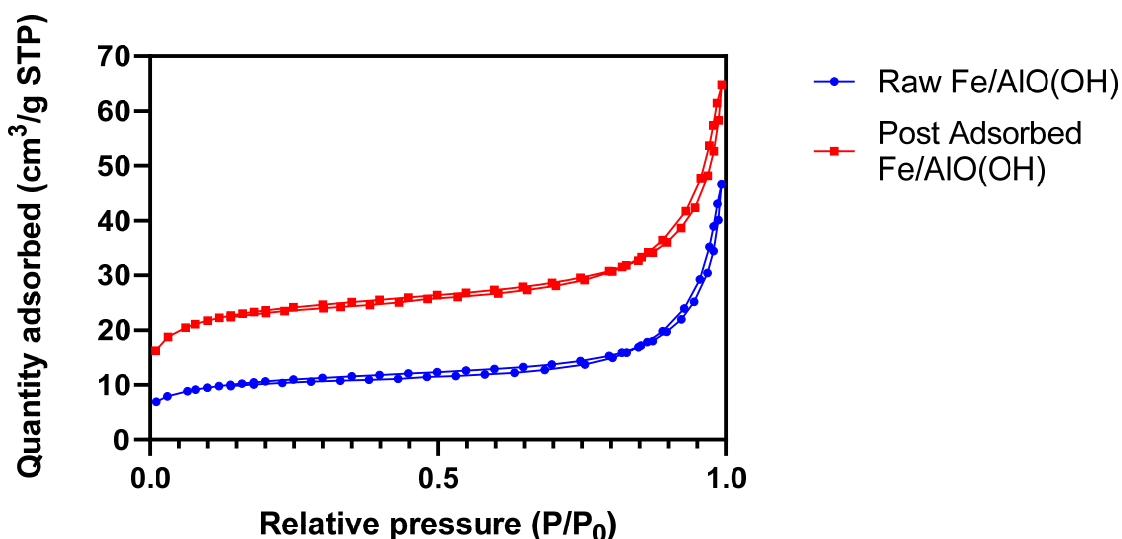


**Figure 7: The nitrogen adsorption-desorption isotherms of Raw Fe/AlO(OH) and As adsorbed Fe/AlO(OH)**

## 3.2 Batch adsorption experiments

The effects of operational parameters (Table 1) on the removal of As(V) from aqueous solution are illustrated in **Figure 8**.
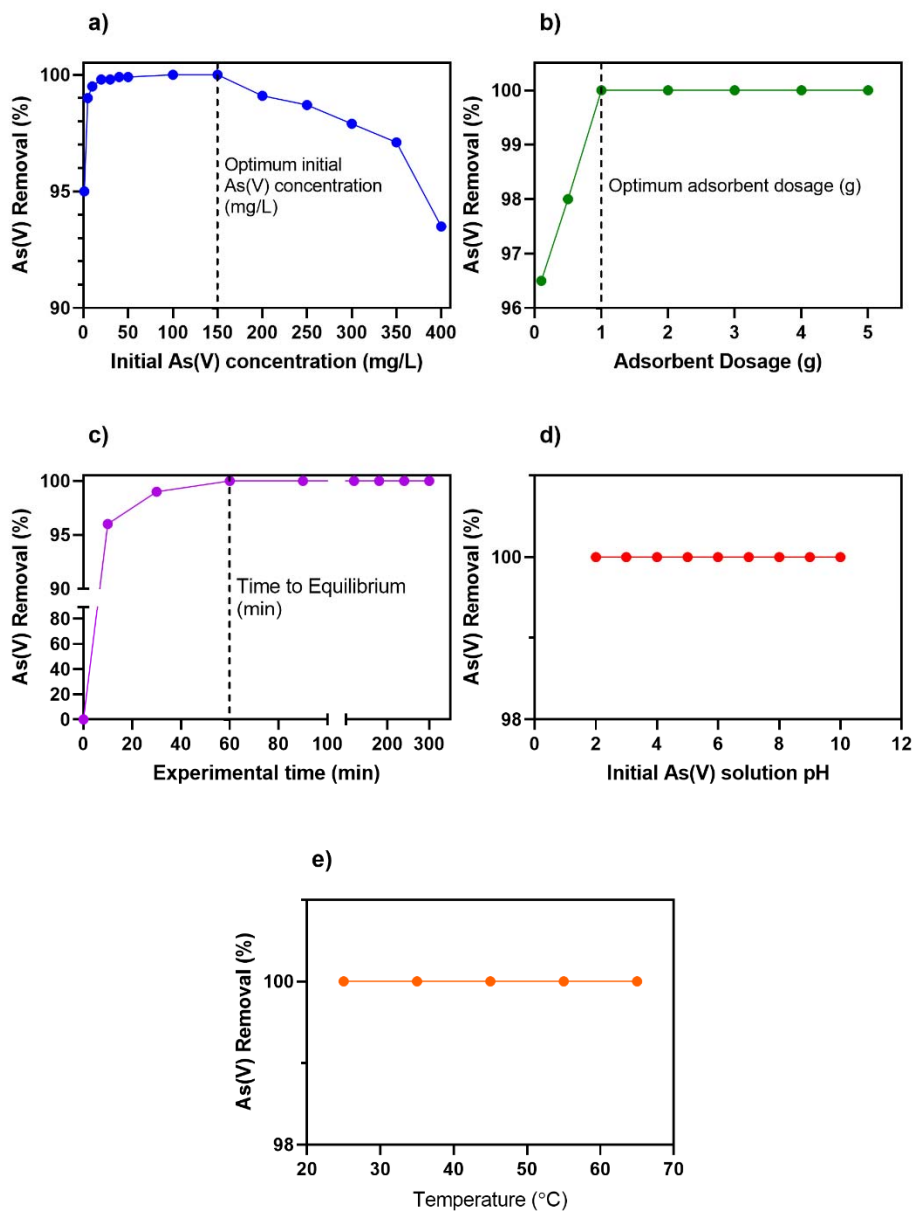
20

**Figure 8 (a-e): Relationship between % removal of As(V) and different operational parameters (see Table 1). Dashed lines indicate the identified optimal conditions for further experiments. To ensure equilibrium conditions all experiments were operated for at least 90 minutes, as confirmed by c).**

### 3.2.1 Effect of initial As(V) concentration

As illustrated in **Figure 8**(a), the effect of initial As(V) concentration demonstrated a complete removal of As(V) from aqueous solution by the Fe/AlO(OH) for concentrations between 1 – 150 mg/L. At 200 mg/L, residual concentration of approximately 1.8 mg/L was measured, thus implying a removal of 99.1 ± 0.05 %. Saturation of the adsorbent was observed at values in excess

21

of 150 mg/L, i.e. the adsorbent did not have enough sites left to accommodate additional As(V) ions. When an adsorbent is saturated with the adsorbate, the rest of the oxyanions, As(V) in this study, are left in solution, hence the decrease in the percentage removal. It can be concluded that an initial As(V) concentration of 150 mg/L is the maximum concentration the Fe/AlO(OH) can accommodate for an adsorbent dose of 1 g. Mostafa et al. [57] reported the optimum concentration being less or equal to 10 mg/L. This study in comparison, demonstrated exceptionally capacity for As(V) adsorption.

### 3.2.2 Effect adsorbent dosage

The effect of adsorbent dosage on the removal of As(V) from aqueous solution was studied; the relationship between dosage and % As(V) removal is illustrated in **Figure 8**(b). It can be noted that a dosage of adsorbent in excess of 1 g is sufficient to ensure complete removal of As(V) from the system for an As(V) concentration of up to 150 mg/L. This complete removal of As(V) shows that the material can adsorb large amounts of As(V) oxyanions. The nearly constant percentage removal observed with an increased dosage is attributed to the overlapping of active sites or saturation of adsorption sites, which reduce the available surface area. The concentration of As(V) ions is less than the surface area of the adsorbent material can accommodate and therefore the material has vacant pores or spaces not covered by As(V) ions [58]. In comparison, Maji et al. (2011) [59] reported a dosage of 15 g iron-oxide-coated natural rock which removed 75 % of a 10 mg/L As(V) solution.
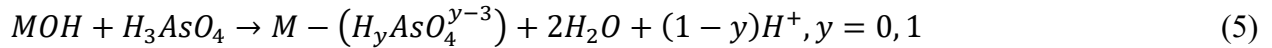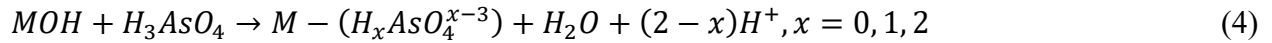
### 3.2.3 Effect of experimental contact time

As shown in **Figure 8**(c), the adsorption of initial concentration As(V) solution by Fe/AlO(OH) is observed as a function of experimental time is shown. The adsorption rapidly proceeds with an agitation time with more than 95% of the adsorption taking place within the initial 60 minutes. A study by Nekhunguni et al. [9] reported that 90 minutes was optimum for removal of As(V) using an iron-based material, in comparison this study demonstrated that a significantly lower contact time of 60 minutes is sufficient for equilibration.

### 3.2.4 Effect of solution pH

The effect of pH on the removal of As(V) from aqueous solution was studied over a pH range of 2 – 10. The relationship between % removal and initial pH is shown in **Figure 8**(d). The initial pH

22

of As(V) solution had negligible effect on the removal of As(V) from water; the adsorption of As(V) by Fe/AlO(OH) was the same at all pH levels of the solution. As(V) oxyanions are more dominant between pH of 2 – 11; at these solution pH values As(V) take the form of dihydrogen arsenate ($H_2AsO_4^-$) and hydrogen arsenate ($HAsO_4^{2-}$). The point of zero charge of Fe/AlO(OH) was found to be pH = 3.02 but exhibited negligible effect on the adsorption of As(V). Liu et al. [60] also reported limited effect of pH on the removal of As(V) using iron and aluminium binary oxide.

To elucidate the mechanism responsible for the lack of pH effect on the adsorption behaviour of As(V) by Fe/AlO(OH), it is necessary to consider the chemistry of the adsorption process. It is widely accepted that As(V) forms strong inner-sphere complexes on Fe and Al oxides [48,50]. This mechanism was verified for FeOOH [61] and AlOOH [62] using X-ray and IR spectroscopy, respectively. Inner sphere complexation involves the specific complexation of the As(V) oxyanions with the adsorbent surface in which surface complexes are formed in either mononuclear/monodentate, mononuclear/bidentate, or binuclear/bidentate configurations [50]. Equation 4 and equation 5 illustrate inner-sphere monodentate and bidentate adsorption of As(V) ions on Fe/AlO(OH), respectively [50]:

$$MOH + H_3AsO_4 \rightarrow M - (H_xAsO_4^{x-3}) + H_2O + (2 - x)H^+, x = 0, 1, 2 \tag{4}$$

$$MOH + H_3AsO_4 \rightarrow M - (H_yAsO_4^{y-3}) + 2H_2O + (1 - y)H^+, y = 0, 1 \tag{5}$$

Where M = Fe/Al

The complexation of the As(V) ions with the adsorbent (MOH) to form adsorbent – adsorbate complex [$M - (H_{x,y}AsO_4^{x,y-3})$] releases $H^+$ ions to the aqueous medium; this results in a drop in pH of the medium during adsorption. When the pH was measured after As(V) adsorption, it was observed that all the pH levels were between 2 – 3 after adsorption. The point of zero charge of Fe/AlO(OH) (pH = 3.02), indicated that the surface was positively charged at the completion of all adsorption experiments. This resulted in a strong electrostatic attraction with the negative arsenate oxyanions for all the pH values tested [63] – resulting in the lack of significant effect of the pH on the removal of As(V). Consequently, Fe/AlO(OH) displayed high effectiveness in the removal of As(V) from aqueous solution within a wide range of pH (2 – 10), which indicates that

23

the adsorbent has high potential efficiency in treating wastewater to recover drinking water within the industrially applicable pH range 5.5 – 8.5 [64].

### 3.2.5 Effect of temperature

As shown in **Figure 8**(e), temperature has a negligible effect on the adsorption of As(V) onto Fe/AlO(OH). However, it should be noted that an increase in temperature led to an increase in EC, TDS, and Salinity. This behaviour agrees with a decrease in the pH i.e. the low pH is as a result of acidity contributed by Fe/AlO(OH) to the aqueous system, as it was synthesised from AMD at between pH 3 – 5. The results show that Fe/AlO(OH) has the potential to efficiently adsorb As(V) at room temperature with consequent potential economic benefits. In comparison, Nekhunguni et al. [9] reported the optimum adsorption temperature of 53 ºC, while Vieira et al. [65] reported an optimal temperature of 20 ºC.

### 3.3    Adsorption isotherms

The adsorption isotherm data was modelled using several adsorption isotherms from literature [66–68]. A summary of the isotherms modelled as well as the results obtained are presented in Table 6. The most striking observation from Table 6 is that all isotherm models fitted the experimental data with a coefficient of determination $R^2 > 0.99$ and a root-mean-square error RMSE $< 3$ mg.g$^{-1}$. This shows that all isotherm models describe the data sufficiently well and therefore all the models were evaluated in terms of the information that the fitter parameters provide about the adsorption mechanisms and energetic considerations.

The most common isotherm tested in literature is the Langmuir isotherm, originally derived for the monolayer adsorption of gasses on a planer surface [66]. The isotherm is based on the assumptions that a monolayer of adsorbate adsorbs to a homogenous surface with a uniform energy distribution. The fitted parameters from the Langmuir isotherm were the maximum adsorption capacity of the material ($Q_{max}$) and the thermodynamic parameters of adsorption: the standard entropy change of adsorption ($\Delta S^o$) and the standard enthalpy change of adsorption ($\Delta H^o$). The $Q_{max}$ of 102 mg.g$^{-1}$ determined from the Langmuir isotherm is exceptionally high when compared to the highest reported studies on the adsorption of As(V) in literature [69–71]. This indicates a very high affinity of the adsorbent for the adsorbate; i.e. promising performance from an industrial perspective. The positive value for $\Delta S^o = 15.5$ J.mol$^{-1}$.K$^{-1}$ indicates an increase in the randomness

24

at the solid liquid interface, likely due to the displacement of water molecules and $H^+$ ions at the surface resulting in a greater increase in entropy than was lost due to the removal of As(V) from solution [72]. This observation has been linked to inner-sphere complexation on the adsorbent surface [73] and corresponds to the observed drop in pH during adsorption with accompanying proposed adsorption mechanisms (equation 4 and 5). Chaudhry and co-workers [74] also reported a positive entropy change for As(V) adsorption and ascribed this increased to As(V) adsorption releasing $H^+$ ions thereby increasing the freedom within the system. The relatively low $\Delta H^o = 6.35$ kJ.mol$^{-1}$ indicates a physisorption mechanism responsible for adsorption. In physisorption the interaction forces are relatively weak Van der Waals forces and therefore low heats of adsorption of between 5 – 40 kJ/mol are usually measured [75]. Nekhunguni et al [9] measured an equivalently low enthalpy of adsorption for As(V) adsorption to iron (hydr)oxide modified zeolite of 9.392 kJ.mol$^{-1}$. The low enthalpy of adsorption results in a limited dependence on temperature of the system, as predicted by the Van't Hoff equation [76], which is promising for industrial application (corresponding to the limited temperature effect on adsorption). A similar combined adsorption mechanism involving physisorption and inner-sphere complexation was reported by Pintor et al. 2020 [77] for As(V) adsorption on iron coated cork granules. The impact of this combined mechanism is that the adsorption follows a fast, temperature insensitive physisorption mechanism coupled to an inner sphere complexation mechanism which has the potential to inhibit dissolution rates, consequently stabilising the adsorbent at high adsorbate coverage [50]. An important parameter to consider when estimating the Langmuir parameters is the separation factor ($R_L$) [78]. The $R_L$ values give an indication of the favourability of the adsorption, $R_L > 1$ indicates unfavourable adsorption, $R_L = 1$ linear adsorption, $R_L < 1$ favourable adsorption, and $R_L = 0$ irreversible adsorption [79]. For initial concentrations tested in this study the adsorption process is highly favourable; $R_L$ values between 0.0043 and 0.167 were calculated.

The Freundlich isotherm was developed to account for the inhomogeneity of the adsorbent surface. This isotherm does not predict the linear behaviour at low adsorbate concentrations or saturation behaviour at high concentrations [78]. The fitted parameters from the Freundlich isotherm model are the Freundlich constant ($K_F$), the Freundlich intensity parameter ($n_F$). The Freundlich intensity parameter gives an indication of the favourability of the adsorption, with $n_F > 1$ favourable, $n_F = 1$ linear adsorption, and $n_F < 1$ unfavourable adsorption. In this case the $n_F = 3.90$ show a highly favourable adsorption process.

25

The multiple surface Langmuir isotherm was developed in 1918 in the seminal paper on adsorption of gases on surfaces by Irving Langmuir [66]. The isotherm was derived with the assumption that multiple surface types exist on the surface of the adsorbent with different adsorption properties. In the current paper, the number of heterogeneous surface types was limited to two. The results from the non-linear fit showed very similar maximum adsorption capacities for the two surfaces with $Q_{max1} = 67.2$ mg.g$^{-1}$ and $Q_{max2} = 61.9$ mg.g$^{-1}$ (yielding a total maximum adsorption capacity of 129 mg.g$^{-1}$). The energetics of the surfaces were, however, very different, with the standard entropy changes of $\Delta S_1^o = 36.45$ J.mol$^{-1}$.K$^{-1}$ and $\Delta S_2^o = -22.02$ J.mol$^{-1}$.K$^{-1}$. These results indicate that on surface type 1, the randomness increased (likely due to surface complexation), while on surface 2, the randomness decreased; adsorption processes are expected to decrease entropy due to the decrease in randomness in the system. The $\Delta H_1^o = 10.65$ kJ.mol$^{-1}$ and $\Delta H_2^o = 0.588$ kJ.mol$^{-1}$ indicated a weak dependence of the system on temperature. The thermodynamic properties in the two surface Langmuir model as compared to the traditional Langmuir isotherm, as discussed above, indicates that the Langmuir results were a nett effect for the surfaces with different properties. The $0.00177 < R_{L1} < 0.0852$ and $0.0428 < R_{L2} < 0.641$ showed that both surface types were favourable to adsorption.

The Dubinin-Radushkevich (DR) isotherm was originally developed to describe the adsorption of gases and vapours and later modified to predict bisolute adsorption in dilute liquid solution [80]. This equation was later generalised to the Dubinin-Astokov (DA) [81] isotherm to account for more complicated adsorption behaviour. In these adsorption isotherms, the parameters indicated the maximum adsorption capacity of the adsorbents – $Q_{maxDR}$ and $Q_{maxDA}$ (mg/g), the energy required to adsorb an adsorbate from infinity to the adsorbent surface – $E_{DR}$ and $E_{DA}$ (kJ/mol). The maximum adsorbate solubility is represented by $C_S$, and the fitted empirical exponent in the DA isotherm ($n_{DA}$) is a value between $1.5 – 3$. The results from the non-linear fits showed comparable adsorption capacities to the Langmuir and Two-surface Langmuir models ($Q_{maxDR} = 115$ mg/g and $Q_{maxDA} = 125$ mg/g). Similar adsorption energies were determined for the DR and DA isotherms ($E_{DR} = 13.3$ kJ/mol and $E_{DA} = 12.9$ kJ/mol). The energies of adsorption indicate a likely diffusion controlled mechanism responsible for adsorption; E-values < 8 kJ/mol indicate physisorption, E > 16 kJ/mol represent chemisorption, and 8 kJ/mol < E < 16 kJ/mol denote a diffusion controlled adsorption mechanisms [79].

26

Additionally, $E_{DR}$ can be used to estimate the internal surface area of an adsorbent by the empirical equations 6.

$$S_{mi} = \frac{21600 W_o}{\beta E_{DR} - 10.4} \tag{6}$$

In equation 6, $W_o$ is the volume of adsorbed species – $W_o = N_{Ao}.V_m$. $N_{Ao}$ is the maximum molar amount adsorbed in mol/cm$^3$, and $V_m$ is the molar volume of the adsorbate (cm$^3$/mol). $\beta$ is the affinity coefficient of the of the adsorbate relative to a reference – by convention phenol. The results from equation 6 predicted an internal surface are of 31.9 m$^2$/g, which is very close to the surface area of 37.6 m$^2$/g measured by BET method (Table 5).

**Table 6: Summary of the adsorption isotherms tested, the fitted parameters, and the coefficient of determination (R$^2$) and root-mean-square error (RMSE) as a measure of the goodness of fit of the different isotherm models.**

| Isotherm | Differential form | Fitted Parameters | R$^2$/RMSE |
|---|---|---|---|
| Langmuir [66–68] | $Q_e = \dfrac{k_L(T)Q_{max}C_e}{1 + k_L(T)C_e}$, $\quad k_L(T) = \exp\left(\dfrac{\Delta S^o}{R} - \dfrac{\Delta H^o}{RT}\right)$ | $\Delta S^o = 15.5\dfrac{J}{mol.K}$ $\Delta H^o = 6.35\dfrac{kJ}{mol}$ $Q_{max} = 102\dfrac{mg}{g}$ $0.0043 < R_L < 0.167$ | 0.994/ 2.45 mg.g$^{-1}$ |
| Freundlich [67] | $Q_e = K_F(T)C_e^{\frac{1}{n}}$ | $K_F(298\,K)$ $= 45.5\dfrac{mg}{g}\left(\dfrac{L}{mg}\right)^{\frac{1}{n_F}}$ $K_F(308\,K)$ $= 46.4\dfrac{mg}{g}\left(\dfrac{L}{mg}\right)^{\frac{1}{n_F}}$ $K_F(318\,K)$ $= 46.7\dfrac{mg}{g}\left(\dfrac{L}{mg}\right)^{\frac{1}{n_F}}$ $n_F = 3.90$ | 0.997/ 1.76 mg.g$^{-1}$ |
| Two-surface Langmuir [66] | $Q_e = \displaystyle\sum_{i=1}^{2}\dfrac{k_{L,i}(T)Q_{max,i}C_e}{1 + k_{L,i}(T)C_e}$, | $\Delta S_1^o = 36.5\dfrac{J}{mol.K}$ | 0.999/ 0.824 mg.g$^{-1}$ |

| | | | |
|---|---|---|---|
| | $$k_{L,i}(T) = \exp\left(\frac{\Delta S_i^o}{R} - \frac{\Delta H_i^o}{RT}\right)$$ | $\Delta H_1^o = 10.7\frac{kJ}{mol}$, $Q_{max,1} = 67.2\frac{mg}{g}$, $\Delta S_2^o = -22.0\frac{J}{mol.K}$ $\Delta H_1^o = 0.588\frac{kJ}{mol}$ $Q_{max,1} = 61.9\frac{mg}{g}$ $0.00177 < R_L < 0.0852$ $0.0428 < R_L < 0.641$ | |
| Dubinin-Radushkevich [67] | $$Q_e = Q_{max,DR} \exp\left\{-\left[\frac{RTln(C_S/C_e)}{E_{DR}}\right]^2\right\}$$ | $E_{DR} = 13.3\frac{kJ}{mol}$, $Q_{max} = 115\frac{mg}{g}$ | 0.993/ 2.70 mg.g$^{-1}$ |
| Dubinin-Astokov [67] | $$Q_e = Q_{max,DA} \exp\left\{-\left[\frac{RTln(C_S/C_e)}{E_{DA}}\right]^{n_{DA}}\right\}$$ | $E_{DA} = 12.9\frac{kJ}{mol}$ $Q_{max} = 125\frac{mg}{g}$ $n_{DA} = 1.66$ | 0.993/ 2.62 mg.g$^{-1}$ |

## 3.4   Adsorption Kinetics

Adsorption kinetics for the current study was determined to elucidate the mechanisms and rates of adsorption of As(V) by the Fe/AlO(OH); Table 7 summarises the kinetic models tested. The resulting non-linear fitted parameters are shown in Table 8 and the resulting fits for the different models are shown graphically in Figure 9. The shaded areas in Figure 9 show the 99% prediction bands for the respective fits; prediction bands are those areas with a 99% probability of containing future observations [82].

The most common adsorption kinetics traditionally tested is the Lagergren pseudo first order (PFO) model [78]. This model was developed to predict the adsorption of soluble substances from solution by S.K. Lagergren in 1898. Despite its ubiquitous application, this model suffers from serious drawbacks in terms of application and interpretation of the fitted results [78]. The most serious of these being the dependence of the fitted parameter $k_1$ on the initial concentration of the

28

adsorption experiment. This means that the model cannot be applied to unknown initial concentration conditions which limits the application to batch systems – preventing application in continuous flow systems due to incompatibility with continuous mole balance equations [76]. The results from the non-linear regressions (Table 8) show very good fits were obtained for the PFO model ($R^2$ = 0.987 – 1.00), however the 99% prediction bands shows extremely large uncertainty in the location of future observations – in the case of the 250 mg.L$^{-1}$ initial As(V) concentration, future observations have a 99% probability of falling in a region defined by 62.5±11.3 mg.g$^{-1}$. This is an interval size 22.6 mg.g$^{-1}$ on an average value of 62.5 mg.g$^{-1}$ (36% of the average). This extremely large uncertainty makes application of the kinetic model extremely risky.

The pseudo second order (PSO) model was derived by a similar method as the PFO model, with the exception that the model is described by a second order dependence on the adsorbed amount [83]. This model suffers from the same limitation as that for the PFO model, i.e. $k_1$ is a function of the initial pollutant concentration and therefore extrapolation of the results are limited. As was the case for the PFO model, the PSO model fit the results well ($R^2$ = 0.987 – 1.00), but unfortunately an unacceptably large prediction interval was observed (250 mg.L$^{-1}$: 61.0 ± 8.18 mg.g$^{-1}$, i.e. 26.8% of the average).

The two-phase adsorption (TPA) model was derived on the basis of two parallel adsorption processes, a rapid and a slow adsorption mechanism [84–86]. This model provides an improvement on the PFO and PSO models, however, there remains uncertainty in the value of $Q_e$ and therefore extrapolation of the model remains problematic. The results from the fitting procedure show good agreement with the experimental results $R^2$ = 0.995.

The Langmuir kinetic model was derived from the reversible surface reaction described by equation 7 and the reversible rate expression (equation 8):

$$A + S \leftrightharpoons A^*\tag{7}$$

$$r_A = \frac{dQ}{dt} = k_{ad}C_A\theta - k_{de}(1-\theta) = k_{ad}C_A\left(1 - \frac{Q_t}{Q_{max}}\right) - k_{de}\frac{Q_t}{Q_{max}}\tag{8}$$

In equation 7 and 8, $A$ represents an adsorbate species, $S$ represents an available surface site for adsorption, $A^*$ represents an adsorbed species, $r_A$ represents the rate of adsorption (mg.g$^{-1}$.min$^{-1}$), $k_{ad}$ is the adsorption kinetic rate constant (L.g$^{-1}$.min$^{-1}$) and $k_{de}$ the desorption rate constant (min$^{-1}$).

29

By setting $r_A = 0$, the Langmuir adsorption isotherm can be obtained from equation 8 and therefore the desorption rate constant can be determined from the Langmuir equilibrium constant ($K_L$): $k_{de} = k_{ad}/K_L$. The power of the Langmuir kinetic expression is that the entire system is described by a single kinetic parameter ($k_{ad}$) and the temperature dependence can be determined from the thermodynamic parameters fitted in the Langmuir isotherm model. The results from the non-linear fit in Table 8 show a very good fit ($R^2 = 0.995$), especially considering the data was fit by a single kinetic parameter. In addition, the prediction interval for the Langmuir kinetic model was significantly smaller than that observed for the PFO, PSO, and TPA models. The model is also compatible with the continuous mole balances [76] and could therefore for used to predict the behaviour of the system during continuous operation.

To account for pore diffusion in adsorption systems, the Crank diffusion model was derived using the assumption that homogeneous diffusion took place in a sphere with a constant diffusivity (De). The resulting model is shown in Table 7. The analytical solution containing the infinite series was solved by iterative solution until the contribution of the consecutive terms were less than a set limiting value ($<10^{-8}$). The results from this non-linear fit shows good agreement with the experimental data ($R^2 = 0.996$), however, as with the TPA model uncertainty exist in the value of $Q_e$ and therefore the extrapolation should be done with care. The resulting $k_{CR}$ provides significant insight into the factors dominating the reaction rates in the system. In this case the $k_{CR} = 0.00387$ min$^{-1}$ represents an effective diffusivity $D_e = 6.60 \times 10^{-14}$ m$^2$.s$^{-1}$. When compared to the molecular diffusivity of arsenate of $D = 8.75 \times 10^{-10}$ m$^2$.s$^{-1}$ [87] it is clear than the internal structure of the adsorbent has a significantly limiting effect on the internal diffusion within the adsorbent particle.

The Weber-Morris intraparticle diffusion model has traditionally been used to estimate the effect of interparticle and intraparticle diffusion on the adsorption of pollutants [78]. This model provides an indication of the different phases of adsorption seen in the multilinear fit of the data, with the first phase indicating intraparticle diffusion, the second phase intraparticle, and the final phase the adsorption onto the adsorbent [88]. The a good fit of the data was obtained ($R^2 = 0.998$) and the results indicated $D_e$ values between $2.25 \times 10^{-15}$ and $6.60 \times 10^{-14}$ m$^2$.s$^{-1}$, demonstrating the severity of the diffusion limitations in the system.

**Table 7: Summary of kinetic models used to analyse As(V) adsorption on Fe/AlO(OH)**

| Kinetic Law | Differential form | Analytical form | Model Parameters | Notes |
|---|---|---|---|---|
| Pseudo first order [68] | $\dfrac{dQ}{dt} = k_1(Q_e - Q)$ | $Q = Q_e(1 - e^{-k_1 t})$ | $Q_e$, $k_1$ | $Q_e$ and $k_1$ are solved for each $C_0$ |
| Pseudo second order [68] | $\dfrac{dQ}{dt} = k_1(Q_e - Q)^2$ | $Q = \dfrac{(k_1 Q_e^2)t}{1 + k_1 Q_e t}$ | $Q_e$, $k_1$ | $Q_e$ and $k_1$ are solved for each $C_0$ |
| Two phase adsorption [84–86] | $\dfrac{dQ_{slow}}{dt} = k_{fast}Q_{fast} - k_{slow}Q_{slow}$<br><br>$Q = Q_{fast} + Q_{slow}$ | $Q = Q_{fast}(1 - e^{-k_{fast}t})$<br>$+ (Q_e - Q_{fast})$<br>$(1 - e^{-k_{slow}t})$ | $Q_{fast}$, $k_{fast}$, $Q_e$, $k_{slow}$ | $Q_e$ for each $C_0$. Global $Q_{fast}$, $k_{fast}$, and $k_{slow}$ fitted |
| Langmuir adsorption [89] | $\dfrac{dQ}{dt} = k_{ad}C(Q_{max} - Q) - \dfrac{k_{ad}}{K_L}Q$ | | $k_{ad}$, $Q_{max}$, $K_L$ | Global $k_1$ fitted $Q_{max}$ and $k_L$ from Langmuir isotherm |
| Crank internal mass transfer model [68] | $\dfrac{\partial Q}{\partial t} = k_{CR}\dfrac{\partial}{\partial r}\left(r^2\dfrac{\partial Q}{\partial r}\right)$<br><br>$k_{CR} = \dfrac{D_e}{r^2}$ | $\dfrac{Q}{Q_e} = \dfrac{6}{\pi^2}\sum_{n=1}^{\infty}\dfrac{1}{n^2}\exp(-k_{CR}n^2\pi^2 t)$ | $k_{CR}$, $Q_e$ | $Q_e$ for each $C_0$. Global $k_{CR}$ fitted |
| Weber and Morris [68,90] | | $Q = \dfrac{k_{WM}}{Q_e}t^{\frac{1}{2}} + C,$<br><br>$k_{WM} = \dfrac{6}{\pi^{\frac{1}{2}}}\sqrt{\dfrac{D_e}{r^2}} = \dfrac{6}{\pi^{\frac{1}{2}}}\sqrt{k_i}$ | $\dfrac{D_e}{r^2}$, $Q_e$, $C$ | $Q_e$ fitted for each $C_0$. Three global $k_{WM}$ fitted. |

**Table 8: Kinetic parameter fits for the kinetic models described in Table 7**

| Kinetic Law | Fitted Parameters | | | | | | | | | | | |
|---|---|---|---|---|---|---|---|---|---|---|---|---|

**Pseudo first order [68]**

| | 10 ppm | | | 150 ppm | | | 200 ppm | | | 250 ppm | | |
|---|---|---|---|---|---|---|---|---|---|---|---|---|
| | $Q_e$ (mg.g$^{-1}$) | $k_1$ (min$^{-1}$) | R$^2$/RMSE | $Q_e$ (mg.g$^{-1}$) | $k_1$ (min$^{-1}$) | R$^2$/RMSE | $Q_e$ (mg.g$^{-1}$) | $k_1$ (min$^{-1}$) | R$^2$/RMSE | $Q_e$ (mg/g) | $k_1$ (min$^{-1}$) | R$^2$/RMSE |
| | 2.5 | 0.317 | 1.00/0.0152 | 37.5 | 0.590 | 0.999/0.438 | 50 | 0.0486 | 0.985/2.36 | 62.5 | 0.0575 | 0.987/2.82 |

**Pseudo second order [68]**

| | 10 ppm | | | 150 ppm | | | 200 ppm | | | 250 ppm | | |
|---|---|---|---|---|---|---|---|---|---|---|---|---|
| | $Q_e$ (mg.g$^{-1}$) | $k_1$ (g.mg$^{-1}$.min$^{-1}$) | R$^2$/RMSE | $Q_e$ (mg.g$^{-1}$) | $k_1$ (g.mg$^{-1}$.min$^{-1}$) | R$^2$/RMSE | $Q_e$ (mg.g$^{-1}$) | $k_1$ (g.mg$^{-1}$.min$^{-1}$) | R$^2$/RMSE | $Q_e$ (mg.g$^{-1}$) | $k_1$ (g.mg$^{-1}$.min$^{-1}$) | R$^2$/RMSE |
| | 2.5 | 0.896 | 1.00/0.0104 | 37.5 | 0.00672 | 0.999/1.71 | 50 | 0.00316 | 0.985/2.19 | 62.5 | 0.00320 | 0.987/2.01 |

**Two phase adsorption [84–86]**

| 10 ppm | 150 ppm | 200 ppm | 250 ppm | Global | | | |
|---|---|---|---|---|---|---|---|
| $Q_e$ (mg.g$^{-1}$) | | | | $Q_{fast}$ (mg.g$^{-1}$) | $k_{fast}$ (min$^{-1}$) | $k_{slow}$ (min$^{-1}$) | R$^2$/RMSE |
| 2.5 | 37.5 | 50 | 62.5 | 5.815 | 0.1346 | 0.0510 | 0.995/1.718 |

**Langmuir adsorption [89]**

| Global | | | | |
|---|---|---|---|---|
| $k_{ad}$ (L.g$^{-1}$.min$^{-1}$) | $Q_{max}$ (mg.g$^{-1}$)[‡] | $\Delta H^o$ (kJ.mol$^{-1}$)[‡] | $\Delta S^o$ (J.mol$^{-1}$.K$^{-1}$)[‡] | R$^2$/RMSE |
| 0.0565 | 102 | 6.35 | 15.5 | 0.995/1.73 |

**Crank model [68]**

| 10 ppm | 150 ppm | 200 ppm | 250 ppm | Global | |
|---|---|---|---|---|---|
| $Q_e$ (mg.g$^{-1}$) | | | | $k_{CR}$ (min$^{-1}$) | R$^2$/RMSE |
| 2.5 | 37.5 | 50 | 62.5 | 0.00387 | 0.996/1.48 |

**Weber and Morris [68,90]**

| 10 ppm | | | | 150 ppm | | | | 200 ppm | | | | 250 ppm | | | | Global | | | |
|---|---|---|---|---|---|---|---|---|---|---|---|---|---|---|---|---|---|---|---|
| $Q_e$ | $C_1$ | $C_2$ | $C_3$ | $Q_e$ | $C_1$ | $C_2$ | $C_3$ | $Q_e$ | $C_1$ | $C_2$ | $C_3$ | $Q_e$ | $C_1$ | $C_2$ | $C_3$ | $k_1$ | $k_2$ | $k_3$ | R$^2$/RMSE |
| (mg.g$^{-1}$) | | | | (mg.g$^{-1}$) | | | | (mg.g$^{-1}$) | | | | (mg.g$^{-1}$) | | | | min$^{-1}$ | | | |
| 2.5 | 0 | 1.84 | 2.66 | 37.5 | 0 | 24.4 | 37.5 | 50 | 0 | 29.5 | 49.9 | 62.5 | 0 | 38.2 | 61.9 | 0.00387 | 0.000132 | 0.00 | 0.998/0.969 |

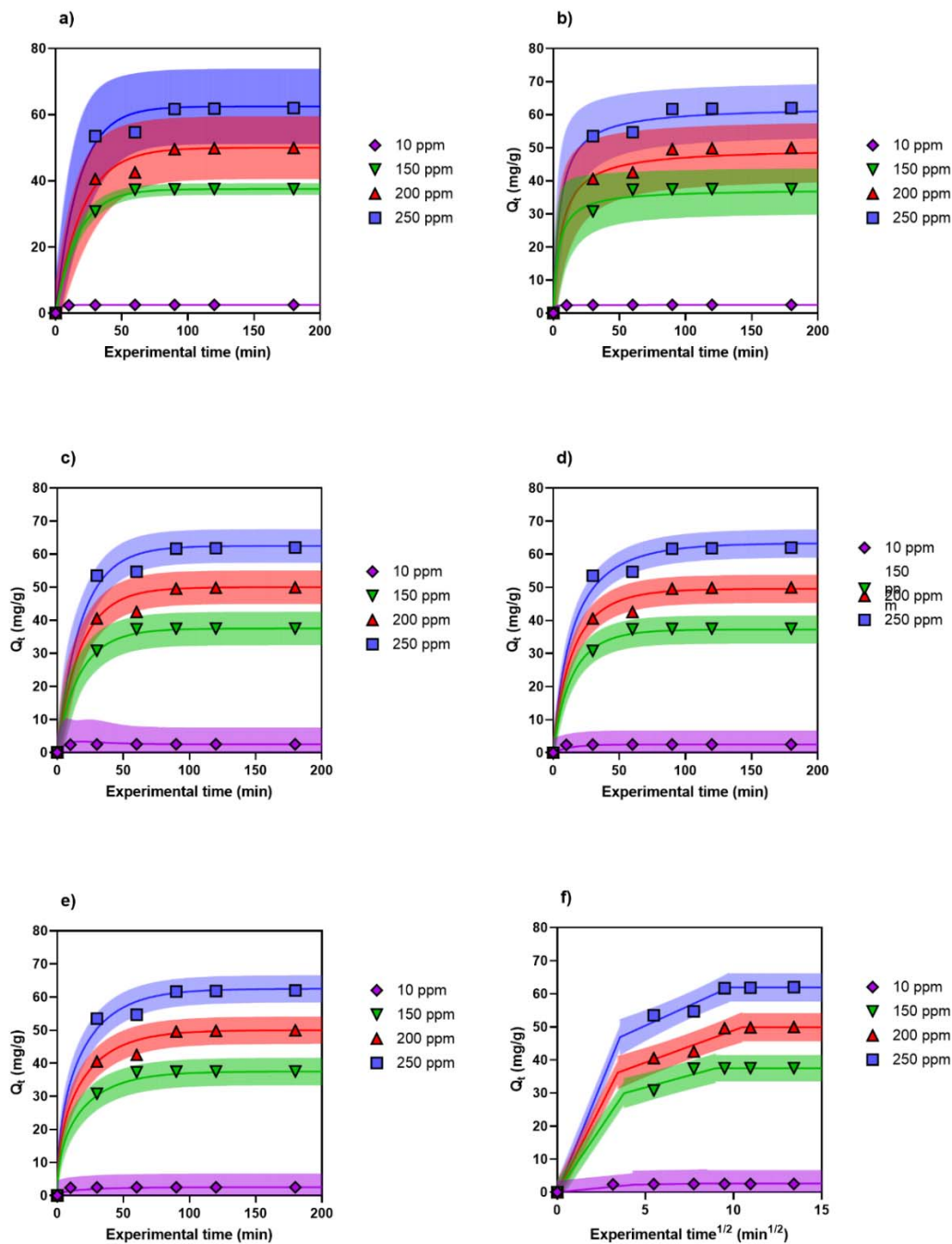[‡] From Langmuir Isotherm (Table 6)

32

**Figure 9: Kinetic fits of the models summarized in Table** 7 **for the adsorption of As(V) to Fe/AlO(OH). The figures represents a) Pseudo first order, b) Pseudo second order, c) Two phase adsorption, d) Langmuir adsorption, e) Crank model, f) Webber and Morris model. The shaded regions indicate the 99% prediction intervals for each initial concentration of As(V).**

## 3.5 Regeneration study

A regeneration study was conducted to evaluate the ability of the synthesised Fe/AlO(OH) to be recovered and reused after As(V) adsorption. The % recovery of the material is illustrated in Figure 10.
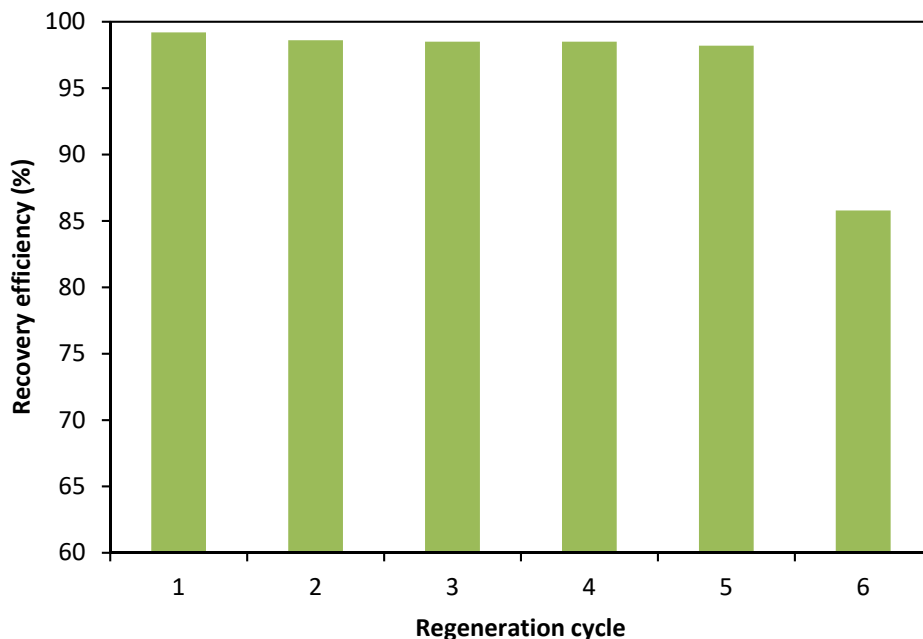


**Figure 10: Recovery efficiency of As(V) from Fe/AlO(OH)**

Figure 10 showed that the first five regeneration cycles show outstanding recovery of the adsorbent (Fe/AlO(OH)). This could be due to the intact covalent bonding that still holds its composition in place. After the 5th cycle, a significant decline in the recovery is noted. This could be due to the strong ionic bond between oxygen (from arsenate) and metal (iron/aluminium) making it difficult to separate the atoms [50,63].

## 3.6 Comparison of Fe/AlO(OH) with other adsorbents

A comparison of adsorption capacities ($Q_e$) between Fe/AlO(OH) and other Fe and/or Al-based adsorbents was done. From the comparison shown in Table 9 can be concluded that the synthesised Fe/AlO(OH) showed the highest known adsorption capacity for As(V).

34

**Table 9: Comparison of Fe/AlO(OH) with other Al and Fe based adsorbents for As removal**

| Adsorbent | Pollutant | $Q_e$ (mg.g$^{-1}$) | $C_o$ (mg.L$^{-1}$) | pH | References |
|---|---|---|---|---|---|
| Fe/AlO(OH) | Arsenic | 102 | 150 | No effect | This study |
| Iron (hydr)oxide modified zeolite | Arsenic | 1.69 | 10 | No effect | Nekhunguni et al., [9] |
| Magnetite | Arsenic | 7.69 | 30 | 6 | Shahid et al. [91] |
| Iron-coated seaweeds | Arsenic | 7.3 | 10 | 7 | Vieira et al. [65] |
| FeOOH/γ-Al$_2$O$_3$ granules | Arsenic | 4.264 | 10 | 4 | Wang et al. [44] |
| Goethite | Arsenic and selenium | 7.740 | 0.150 | 4 | Jacobson and Fan [92] |
| Modified montmorillorite | Arsenic | 16.13 | 35 | 2 – 10 | Ren et al. [69] |
| Aluminium (hydr) oxide coated red scoria and pumice | Arsenic | 2.68 | 1.028 | 7 | Asere et al. [21] |
| Nano aluminium doped manganese copper ferrite polymer | Arsenic | 0.053 | 0.1 | Not optimised | Malana et al. [79] |
| Fe$_3$O$_4$@SiO$_2$@TiO$_2$ nanoabsorbent | Arsenic | 21.3 | 100 | 9 | Feng et al. [70] |
| Manganese ferrite nanoparticles | Arsenic | 27.65 | 5 | 2 | Martinez–Vargas et al. [71] |
| Magnetite-maghemite nanoparticles | Arsenic and chromium | 3.71 | 1.5 | 2 | Chowdhury and Yanful [22] |

The results shown in Table 9 are noteworthy as most other adsorbents were synthesized from synthetic chemicals whereas Fe/AlO(OH) was recovered from authentic AMD, illustrating the importance of this study.

## 4. Conclusions

This study demonstrated the successful synthesis of Aluminium enriched Ferric oxide-hydroxide (Fe/AlO(OH)) from authentic AMD via fractional precipitation. The synthesized Fe/AlO(OH) exhibited the highest known adsorption capacity for As(V) of 102 mg.g$^{-1}$ (estimated by the Langmuir isotherm model). Batch adsorption experiments revealed optimal conditions for the removal of As(V) (>99% As(V) removal) from an aqueous system: 150 mg.L$^{-1}$ of As(V) concentration, 1 g adsorbent, and 60 min equilibration time. As(V) removal was found independent of pH and temperature. The removal of As(V) was successfully modelled ($R^2 > 0.99$) by the Langmuir-, Freundlich-, Two surface Langmuir-, Dubinin-Radushkevich-, and Dubinin-Astokov isotherm models isotherm models. These models showed that favourable adsorption took place on a heterogenous surface with very similar properties. The adsorption mechanism was identified as a combination of physisorption and mass transfer limited adsorption involving inner-sphere complexation on the adsorbent surface with concomitant release of H$^+$ (drop in pH and positive $\Delta S^o$), while being insensitive to temperature (small $\Delta H^o$). The Langmuir kinetic model was able to successfully model the kinetics of adsorption ($R^2 = 0.995$) for all As(V) concentrations (10 – 250 mg.L$^{-1}$) using a single reaction rate constant and the Langmuir isotherm thermodynamic parameters. Regeneration showed outstanding recovery of the adsorbent after five cycles, thereby showing marked potential in the reusability of the material. This double-edged study demonstrated the feasibility of valorisation of AMD by recovering valuable di-metals and employing them to curtail the impact of problematic pollutants.

## Acknowledgement

## References

[1]    M. Edelstein, M. Ben-Hur, Heavy metals and metalloids: Sources, risks and strategies to reduce their accumulation in horticultural crops, Sci. Hortic. (Amsterdam). 234 (2018) 431–444. https://doi.org/10.1016/j.scienta.2017.12.039.

[2] R.N. Ratnaike, Acute and chronic arsenic toxicity, Postgrad. Med. J. 79 (2003) 391–396. https://doi.org/10.1136/pmj.79.933.391.

[3] J. Singh, A.S. Kalamdhad, Effects of Heavy Metals on Soil, Plants, Human Health and Aquatic Life, Int. J. Res. Chem. Environ. 1 (2011) 15–21. https://www.researchgate.net/publication/265849316_Effects_of_Heavy_Metals_on_Soil_Plants_Human_Health_and_Aquatic_Life.

[4] R. Singh, S. Singh, P. Parihar, V.P. Singh, S.M. Prasad, Arsenic contamination, consequences and remediation techniques: A review, Ecotoxicol. Environ. Saf. 112 (2015) 247–270. https://doi.org/10.1016/j.ecoenv.2014.10.009.

[5] World Health Organization, World health statistics 2011, Geneva, 2011.

[6] K. Simeonidis, T. Gkinis, S. Tresintsi, C. Martinez-Boubeta, G. Vourlias, I. Tsiaoussis, G. Stavropoulos, M. Mitrakas, M. Angelakeris, Magnetic separation of hematite-coated Fe3O4 particles used as arsenic adsorbents, Chem. Eng. J. 168 (2011) 1008–1015. https://doi.org/10.1016/j.cej.2011.01.074.

[7] U.S. EPA, Public Access to the Toxics Release Inventory ( TRI ), Washington, D.C., 2001.

[8] Sabs Standards Division, SANS 241-1: 2011 SOUTH AFRICAN NATIONAL STANDARD Drinking water Part 1 : Microbiological, physical, aesthetic, 2011.

[9] P.M. Nekhunguni, N.T. Tavengwa, H. Tutu, Investigation of As(V) removal from acid mine drainage by iron (hydr) oxide modified zeolite, J. Environ. Manage. 197 (2017) 550–558. https://doi.org/10.1016/j.jenvman.2017.04.038.

[10] M.F. Naujokas, B. Anderson, H. Ahsan, H. Vasken Aposhian, J.H. Graziano, C. Thompson, W.A. Suk, The broad scope of health effects from chronic arsenic exposure: Update on a worldwide public health problem, Environ. Health Perspect. 121 (2013) 295–302. https://doi.org/10.1289/ehp.1205875.

[11] C. Abernathy, Exposure and Health Effects, Arsen. Drink. Water. (2001) 100.

[12] B.A. Fowler, C.H.S.J. Chou, R.L. Jones, D.W. Sullivan, C.J. Chen, Arsenic, Fourth Edi,

37

Elsevier, 2015. https://doi.org/10.1016/B978-0-444-59453-2.00028-7.

[13]  R.L. Hendricks, F.B. Reisbick, E.J. Mahaffey, D.B. Roberts, M.N.A. Peterson, Chemical Composition of Sediments and Interstitial Brines from the Atlantis II, Discovery and Chain Deeps, in: Hot Brines Recent Heavy Met. Depos. Red Sea, Springer Berlin Heidelberg, Berlin, Heidelberg, 1969: pp. 407–440. https://doi.org/10.1007/978-3-662-28603-6_39.

[14]  H. Li, H. Li, Y. Li, Y. Liu, Z. Zhao, Blood Mercury, Arsenic, Cadmium, and Lead in Children with Autism Spectrum Disorder, Biol. Trace Elem. Res. 181 (2018) 31–37. https://doi.org/10.1007/s12011-017-1002-6.

[15]  C.G. Lee, P.J.J. Alvarez, A. Nam, S.J. Park, T. Do, U.S. Choi, S.H. Lee, Arsenic(V) removal using an amine-doped acrylic ion exchange fiber: Kinetic, equilibrium, and regeneration studies, J. Hazard. Mater. 325 (2017) 223–229. https://doi.org/10.1016/j.jhazmat.2016.12.003.

[16]  S.A. Schmidt, E. Gukelberger, M. Hermann, F. Fiedler, B. Großmann, J. Hoinkis, A. Ghosh, D. Chatterjee, J. Bundschuh, Pilot study on arsenic removal from groundwater using a small-scale reverse osmosis system—Towards sustainable drinking water production, J. Hazard. Mater. 318 (2016) 671–678. https://doi.org/10.1016/j.jhazmat.2016.06.005.

[17]  C. Hu, Q. Chen, H. Liu, J. Qu, Coagulation of methylated arsenic from drinking water: Influence of methyl substitution, J. Hazard. Mater. 293 (2015) 97–104. https://doi.org/10.1016/j.jhazmat.2015.03.055.

[18]  J.B. Lin, S. Yuan, W. Wang, Z.H. Hu, H.Q. Yu, Precipitation of organic arsenic compounds and their degradation products during struvite formation, J. Hazard. Mater. 317 (2016) 90–96. https://doi.org/10.1016/j.jhazmat.2016.05.057.

[19]  C.S. Fan, S.C. Tseng, K.C. Li, C.H. Hou, Electro-removal of arsenic(III) and arsenic(V) from aqueous solutions by capacitive deionization, J. Hazard. Mater. 312 (2016) 208–215. https://doi.org/10.1016/j.jhazmat.2016.03.055.

[20]  X.H. Guan, J. Wang, C.C. Chusuei, Removal of arsenic from water using granular ferric hydroxide: Macroscopic and microscopic studies, J. Hazard. Mater. 156 (2008) 178–185.

https://doi.org/10.1016/j.jhazmat.2007.12.012.

[21]   T.G. Asere, J. De Clercq, K. Verbeken, D.A. Tessema, F. Fufa, C. V. Stevens, G. Du Laing, Uptake of arsenate by aluminum (hydr)oxide coated red scoria and pumice, Appl. Geochemistry. 78 (2017) 83–95. https://doi.org/10.1016/j.apgeochem.2016.12.013.

[22]   S.R. Chowdhury, E.K. Yanful, Arsenic and chromium removal by mixed magnetite-maghemite nanoparticles and the effect of phosphate on removal, J. Environ. Manage. 91 (2010) 2238–2247. https://doi.org/10.1016/j.jenvman.2010.06.003.

[23]   M. Pehlivan, S. Simsek, S. Ozbek, B. Ozbek, An extensive study on the synthesis of iron based magnetic aluminium oxide nanocomposites by solution combustion method, J. Mater. Res. Technol. 8 (2019) 1746–1760. https://doi.org/10.1016/j.jmrt.2018.12.005.

[24]   T.P. Braga, I.F. Vasconcelos, J.M. Sasaki, J.D. Fabris, D.Q.L. de Oliveira, A. Valentini, Magnetic composites based on hybrid spheres of aluminum oxide and superparamagnetic nanoparticles of iron oxides, J. Magn. Magn. Mater. 322 (2010) 633–637. https://doi.org/10.1016/j.jmmm.2009.10.028.

[25]   J. Hübner, M. Klaumünzer, M. Comet, C. Martin, L. Vidal, M. Schäfer, C. Kryschi, D. Spitzer, Insights into combustion mechanisms of variable aluminum-based iron oxide/-hydroxide nanothermites, Combust. Flame. 184 (2017) 186–194. https://doi.org/10.1016/j.combustflame.2017.06.006.

[26]   V. Akinwekomi, J.P. Maree, C. Zvinowanda, V. Masindi, Synthesis of magnetite from iron-rich mine water using sodium carbonate, J. Environ. Chem. Eng. 5 (2017) 2699–2707. https://doi.org/10.1016/j.jece.2017.05.025.

[27]   V. Akinwekomi, J.P. Maree, V. Masindi, C. Zvinowanda, M.S. Osman, S. Foteinis, L. Mpenyana-Monyatsi, E. Chatzisymeon, Beneficiation of acid mine drainage (AMD): A viable option for the synthesis of goethite, hematite, magnetite, and gypsum – Gearing towards a circular economy concept, Miner. Eng. 148 (2020) 106204. https://doi.org/10.1016/j.mineng.2020.106204.

[28] M.J. Ryan, A.D. Kney, T.L. Carley, A study of selective precipitation techniques used to recover refined iron oxide pigments for the production of paint from a synthetic acid mine drainage solution, Appl. Geochemistry. 79 (2017) 27–35. https://doi.org/10.1016/j.apgeochem.2017.01.019.

[29] V. Masindi, E. Chatzisymeon, I. Kortidis, S. Foteinis, Assessing the sustainability of acid mine drainage (AMD) treatment in South Africa, Sci. Total Environ. 635 (2018) 793–802. https://doi.org/10.1016/j.scitotenv.2018.04.108.

[30] J.Y. Seo, M.G. Kim, K. Lee, Y.-C. Lee, J.-G. Na, S.G. Jeon, S. Bin Park, Y.-K. Oh, Multifunctional Nanoparticle Applications to Microalgal Biorefinery, in: Ind. Crops Prod., 2017: pp. 59–87. https://doi.org/10.1007/978-3-319-45459-7_4.

[31] V. Masindi, V. Akinwekomi, J.P. Maree, K.L. Muedi, Comparison of mine water neutralisation efficiencies of different alkaline generating agents, J. Environ. Chem. Eng. 5 (2017) 3903–3913. https://doi.org/10.1016/j.jece.2017.07.062.

[32] V. Masindi, Recovery of drinking water and valuable minerals from acid mine drainage using an integration of magnesite, lime, soda ash, $CO_2$ and reverse osmosis treatment processes, J. Environ. Chem. Eng. 5 (2017) 3136–3142. https://doi.org/10.1016/j.jece.2017.06.025.

[33] K.K. Kefeni, T.A.M. Msagati, B.B. Mamba, Acid mine drainage: Prevention, treatment options, and resource recovery: A review, J. Clean. Prod. 151 (2017) 475–493. https://doi.org/10.1016/j.jclepro.2017.03.082.

[34] D.D. Frey, F. Engelhardt, E.M. Greitzer, A role for "one-factor-at-a-time" experimentation in parameter design, Res. Eng. Des. 14 (2003) 65–74. https://doi.org/10.1007/s00163-002-0026-9.

[35] I.D. Smičiklas, S.K. Milonjić, P. Pfendt, S. Raičević, The point of zero charge and sorption of cadmium (II) and strontium (II) ions on synthetic hydroxyapatite, Sep. Purif. Technol. 18 (2000) 185–194. https://doi.org/10.1016/S1383-5866(99)00066-0.

[36] H.N. Tran, F. Tomul, N. Thi Hoang Ha, D.T. Nguyen, E.C. Lima, G.T. Le, C.T. Chang, V. Masindi, S.H. Woo, Innovative spherical biochar for pharmaceutical removal from water: Insight into adsorption mechanism, J. Hazard. Mater. 394 (2020). https://doi.org/10.1016/j.jhazmat.2020.122255.

[37] P. Kumari, P. Sharma, S. Srivastava, M.M. Srivastava, Biosorption studies on shelled Moringa oleifera Lamarck seed powder: Removal and recovery of arsenic from aqueous system, Int. J. Miner. Process. 78 (2006) 131–139. https://doi.org/10.1016/j.minpro.2005.10.001.

[38] S. Bordoloi, S.K. Nath, S. Gogoi, R.K. Dutta, Arsenic and iron removal from groundwater by oxidation-coagulation at optimized pH: Laboratory and field studies, J. Hazard. Mater. 260 (2013) 618–626. https://doi.org/10.1016/j.jhazmat.2013.06.017.

[39] D. Peak, R.G. Ford, D.L. Sparks, An in situ ATR-FTIR investigation of sulfate bonding mechanisms on goethite, J. Colloid Interface Sci. 218 (1999) 289–299. https://doi.org/10.1006/jcis.1999.6405.

[40] M.J. Jiménez-Cedillo, M.T. Olguín, C. Fall, Adsorption kinetic of arsenates as water pollutant on iron, manganese and iron-manganese-modified clinoptilolite-rich tuffs, J. Hazard. Mater. 163 (2009) 939–945. https://doi.org/10.1016/j.jhazmat.2008.07.049.

[41] Y. Yu, L. Yu, K. Shih, J.P. Chen, Yttrium-doped iron oxide magnetic adsorbent for enhancement in arsenic removal and ease in separation after applications, J. Colloid Interface Sci. 521 (2018) 252–260. https://doi.org/10.1016/j.jcis.2018.02.046.

[42] J.J. Friel, C.E. Lyman, Tutorial Review: X-ray Mapping in Electron-Beam Instruments, Microsc. Microanal. 12 (2006) 2–25. https://doi.org/10.1017/S1431927606060211.

[43] Y. Jeong, M. Fan, S. Singh, C.L. Chuang, B. Saha, J. Hans van Leeuwen, Evaluation of iron oxide and aluminum oxide as potential arsenic(V) adsorbents, Chem. Eng. Process. Process Intensif. 46 (2007) 1030–1039. https://doi.org/10.1016/j.cep.2007.05.004.

[44]   Z. Wang, X. Shen, M. Jing, C. Li, Enhanced arsenic removal from drinking water by FeOOH/γ-Al2O3 granules, J. Alloys Compd. 735 (2018) 1620–1628. https://doi.org/10.1016/j.jallcom.2017.11.284.

[45]   D. Cortés-Arriagada, A. Toro-Labbé, Aluminum and iron doped graphene for adsorption of methylated arsenic pollutants, Appl. Surf. Sci. 386 (2016) 84–95. https://doi.org/10.1016/j.apsusc.2016.05.154.

[46]   L. Longa-Avello, C. Pereyra-Zerpa, J.A. Casal-Ramos, P. Delvasto, Study of the calcination process of two limonitic iron ores between 250 °C and 950 °C, Rev. Fac. Ing. 26 (2017) 33–45. https://doi.org/10.19053/01211129.v26.n45.2017.6053.

[47]   Y. Wei, W. Shao, Z. Ma, Z. Chen, W. Lu, Preparation and thermal stability of an atomically sharp Fe/Al interface, Mater. Lett. 185 (2016) 537–540. https://doi.org/10.1016/j.matlet.2016.09.054.

[48]   J.P. Gustafsson, P. Bhattacharya, Geochemical modelling of arsenic adsorption to oxide surfaces, Trace Met. Other Contam. Environ. 9 (2007) 159–206. https://doi.org/10.1016/S1875-1121(06)09006-7.

[49]   M.F. De Lange, T.J.H. Vlugt, J. Gascon, F. Kapteijn, Adsorptive characterization of porous solids: Error analysis guides the way, Microporous Mesoporous Mater. 200 (2014) 199–215. https://doi.org/10.1016/j.micromeso.2014.08.048.

[50]   M.J. Eick, J.D. Peak, W.D. Brady, The Effect of Oxyanions on the Oxalate-Promoted Dissolution of Goethite, Soil Sci. Soc. Am. J. 63 (1999) 1133–1141. https://doi.org/10.2136/sssaj1999.6351133x.

[51]   M. Thommes, K. Kaneko, A. V. Neimark, J.P. Olivier, F. Rodriguez-Reinoso, J. Rouquerol, K.S.W. Sing, Physisorption of gases, with special reference to the evaluation of surface area and pore size distribution (IUPAC Technical Report), 2015. https://doi.org/10.1515/pac-2014-1117.

[52] W. Han, F. Fu, Z. Cheng, B. Tang, S. Wu, Studies on the optimum conditions using acid-washed zero-valent iron/aluminum mixtures in permeable reactive barriers for the removal of different heavy metal ions from wastewater, J. Hazard. Mater. 302 (2016) 437–446. https://doi.org/10.1016/j.jhazmat.2015.09.041.

[53] R. Chitrakar, Y. Makita, A. Sonoda, T. Hirotsu, Fe-Al layered double hydroxides in bromate reduction: Synthesis and reactivity, J. Colloid Interface Sci. 354 (2011) 798–803. https://doi.org/10.1016/j.jcis.2010.11.010.

[54] X. He, X. Qiu, J. Chen, Preparation of Fe(II)–Al layered double hydroxides: Application to the adsorption/reduction of chromium, Colloids Surfaces A Physicochem. Eng. Asp. 516 (2017) 362–374. https://doi.org/10.1016/j.colsurfa.2016.12.053.

[55] K.S.W. Sing, R.T. Williams, Physisorption hysteresis loops and the characterization of nanoporous materials, Adsorpt. Sci. Technol. 22 (2004) 773–782. https://doi.org/10.1260/0263617053499032.

[56] S. Zhang, W. Meng, L. Wang, L. Li, Y. Long, Y. Hei, L. Zhou, S. Wu, Z. Zheng, L. Luo, F. Jiang, Preparation of Nano-Copper Sulfide and Its Adsorption Properties for 17α-Ethynyl Estradiol, Nanoscale Res. Lett. 15 (2020). https://doi.org/10.1186/s11671-020-3274-6.

[57] M.G. Mostafa, Y.H. Chen, J.S. Jean, C.C. Liu, Y.C. Lee, Kinetics and mechanism of arsenate removal by nanosized iron oxide-coated perlite, J. Hazard. Mater. 187 (2011) 89–95. https://doi.org/10.1016/j.jhazmat.2010.12.117.

[58] S. Mandal, M.K. Sahu, R.K. Patel, Adsorption studies of arsenic(III) removal from water by zirconium polyacrylamide hybrid material (ZrPACM-43), Water Resour. Ind. 4 (2013) 51–67. https://doi.org/10.1016/j.wri.2013.09.003.

[59] S.K. Maji, Y.H. Kao, C.W. Liu, Arsenic removal from real arsenic-bearing groundwater by adsorption on iron-oxide-coated natural rock (IOCNR), Desalination. 280 (2011) 72–79. https://doi.org/10.1016/j.desal.2011.06.048.

[60]  R. Liu, W. Gong, H. Lan, T. Yang, H. Liu, J. Qu, Simultaneous removal of arsenate and fluoride by iron and aluminum binary oxide: Competitive adsorption effects, Sep. Purif. Technol. 92 (2012) 100–105. https://doi.org/10.1016/j.seppur.2012.03.020.

[61]  M.L. Farquhar, J.M. Charnock, F.R. Livens, D.J. Vaughan, Mechanisms of arsenic uptake from aqueous solution by interaction with goethite, lepidocrocite, mackinawite, and pyrite: An X-ray absorption spectroscopy study, Environ. Sci. Technol. 36 (2002) 1757–1762. https://doi.org/10.1021/es010216g.

[62]  J. Nordin, P. Persson, A. Nordin, S. Sjöberg, Inner-sphere and outer-sphere complexation of a polycarboxylic acid at the water-boehmite ($\gamma$-AlOOH) interface: A combined potentiometric and IR spectroscopic study, Langmuir. 14 (1998) 3655–3662. https://doi.org/10.1021/la9712449.

[63]  H. Cheng, Y. Hu, J. Luo, B. Xu, J. Zhao, Geochemical processes controlling fate and transport of arsenic in acid mine drainage (AMD) and natural systems, J. Hazard. Mater. 165 (2009) 13–26. https://doi.org/10.1016/j.jhazmat.2008.10.070.

[64]  S.H. Lee, K.W. Kim, B.T. Lee, S. Bang, H. Kim, H. Kang, A. Jang, Enhanced arsenate removal performance in aqueous solution by yttrium-based adsorbents, Int. J. Environ. Res. Public Health. 12 (2015) 13523–13541. https://doi.org/10.3390/ijerph121013523.

[65]  B.R.C. Vieira, A.M.A. Pintor, R.A.R. Boaventura, C.M.S. Botelho, S.C.R. Santos, Arsenic removal from water using iron-coated seaweeds, J. Environ. Manage. 192 (2017) 224–233. https://doi.org/10.1016/j.jenvman.2017.01.054.

[66]  I. Langmuir, The adsorption of gases on plane surfaces of glass, mica and platinum, J. Am. Chem. Soc. 40 (1918) 1361–1403. https://doi.org/10.1021/ja02242a004.

[67]  P. Girods, A. Dufour, V. Fierro, Y. Rogaume, C. Rogaume, A. Zoulalian, A. Celzard, Activated carbons prepared from wood particleboard wastes: Characterisation and phenol adsorption capacities, J. Hazard. Mater. 166 (2009) 491–501. https://doi.org/10.1016/j.jhazmat.2008.11.047.

[68]  L. Largitte, R. Pasquier, A review of the kinetics adsorption models and their application to the adsorption of lead by an activated carbon, Chem. Eng. Res. Des. 109 (2016) 495–504. https://doi.org/10.1016/j.cherd.2016.02.006.

[69]  X. Ren, Z. Zhang, H. Luo, B. Hu, Z. Dang, C. Yang, L. Li, Adsorption of arsenic on modified montmorillonite, Appl. Clay Sci. 97–98 (2014) 17–23. https://doi.org/10.1016/j.clay.2014.05.028.

[70]  C. Feng, C. Aldrich, J.J. Eksteen, D.W.M. Arrigan, Removal of arsenic from gold cyanidation process waters by use of cerium-based magnetic adsorbents, Miner. Eng. 122 (2018) 84–90. https://doi.org/10.1016/j.mineng.2018.03.026.

[71]  S. Martinez–Vargas, A.I. Martínez, E.E. Hernández–Beteta, O.F. Mijangos–Ricardez, V. Vázquez–Hipólito, C. Patiño-Carachure, J. López–Luna, As(III) and As(V) adsorption on manganese ferrite nanoparticles, J. Mol. Struct. 1154 (2018) 524–534. https://doi.org/10.1016/j.molstruc.2017.10.076.

[72]  C.K. Jain, D.C. Singhal, M.K. Sharma, Adsorption of zinc on bed sediment of River Hindon: Adsorption models and kinetics, J. Hazard. Mater. 114 (2004) 231–239. https://doi.org/10.1016/j.jhazmat.2004.09.001.

[73]  T.E. Payne, V. Brendler, M. Ochs, B. Baeyens, P.L. Brown, J.A. Davis, C. Ekberg, D.A. Kulik, J. Lutzenkirchen, T. Missana, Y. Tachi, L.R. Van Loon, S. Altmann, Guidelines for thermodynamic sorption modelling in the context of radioactive waste disposal, Environ. Model. Softw. 42 (2013) 143–156. https://doi.org/10.1016/j.envsoft.2013.01.002.

[74]  S.A. Chaudhry, Z. Zaidi, S.I. Siddiqui, Isotherm, kinetic and thermodynamics of arsenic adsorption onto Iron-Zirconium Binary Oxide-Coated Sand (IZBOCS): Modelling and process optimization, J. Mol. Liq. 229 (2017) 230–240. https://doi.org/10.1016/j.molliq.2016.12.048.

[75]  V.J. Inglezakis, S.G. Poulopoulos, Adsorption, Ion Exchange, and Catalysis, in: Adsorpt. Ion Exch. Catal., Elsevier, 2006: pp. 31–56. https://doi.org/10.1016/B978-044452783-7/50002-1.

[76] H. Scott Fogler, Elements of chemical reaction engineering, Fourth, Pearson Education Limited, London, 2013.

[77] A.M.A. Pintor, B.R.C. Vieira, C.C. Brandaõ, R.A.R. Boaventura, C.M.S. Botelho, Complexation mechanisms in arsenic and phosphorus adsorption onto iron-coated cork granulates, J. Environ. Chem. Eng. 8 (2020) 104184. https://doi.org/10.1016/j.jece.2020.104184.

[78] H.N. Tran, S.J. You, A. Hosseini-Bandegharaei, H.P. Chao, Mistakes and inconsistencies regarding adsorption of contaminants from aqueous solutions: A critical review, Water Res. 120 (2017) 88–116. https://doi.org/10.1016/j.watres.2017.04.014.

[79] M.A. Malana, R.B. Qureshi, M.N. Ashiq, Adsorption studies of arsenic on nano aluminium doped manganese copper ferrite polymer (MA, VA, AA) composite: Kinetics and mechanism, Chem. Eng. J. 172 (2011) 721–727. https://doi.org/10.1016/j.cej.2011.06.041.

[80] M. Jaroniec, A. Deryło, Application of Dubinin—Radushkevich—type equation for describing bisolute adsorption from dilute aqueous solutions on activated carbon, J. Colloid Interface Sci. 84 (1981) 191–195. https://doi.org/10.1016/0021-9797(81)90274-5.

[81] F. Stoeckli, M.V. López-Ramón, C. Moreno-Castilla, Adsorption of phenolic compounds from aqueous solutions, by activated carbons, described by the dubinin - Astakhov equation, Langmuir. 17 (2001) 3301–3306. https://doi.org/10.1021/la0014407.

[82] R.J. Hyndman, G. Athanasopoulos, Forecasting: principles and practice, OTexts, Heathmont, 2018.

[83] L. Largitte, R. Pasquier, New models for kinetics and equilibrium homogeneous adsorption, Chem. Eng. Res. Des. 112 (2016) 289–297. https://doi.org/10.1016/j.cherd.2016.06.021.

[84] M.L. Brusseau, R.E. Jessup, P. Suresh, C. Rao, Nonequilibrium Sorption of Organic Chemicals: Elucidation of Rate-Limiting Processes, Environ. Sci. Technol. 25 (1991) 134–142. https://doi.org/10.1021/es00013a015.

[85] Z. Wang, J. Zhao, L. Song, H. Mashayekhi, B. Chefetz, B. Xing, Adsorption and desorption of phenanthrene on carbon nanotubes in simulated gastrointestinal fluids, Environ. Sci. Technol. 45 (2011) 6018–6024. https://doi.org/10.1021/es200790x.

[86] G. Cornelissen, P.C.M. Van Noort, J.R. Parsons, H.A.J. Govers, Temperature dependence of slow adsorption and desorption kinetics of organic compounds in sediments, Environ. Sci. Technol. 31 (1997) 454–460. https://doi.org/10.1021/es960300+.

[87] M. Tanaka, Y. Takahashi, N. Yamaguchi, K.W. Kim, G. Zheng, M. Sakamitsu, The difference of diffusion coefficients in water for arsenic compounds at various pH and its dominant factors implied by molecular simulations, Geochim. Cosmochim. Acta. 105 (2013) 360–371. https://doi.org/10.1016/j.gca.2012.12.004.

[88] T. Mahlangu, R. Das, L.K. Abia, M. Onyango, S.S. Ray, A. Maity, Thiol-modified magnetic polypyrrole nanocomposite: An effective adsorbent for the adsorption of silver ions from aqueous solution and subsequent water disinfection by silver-laden nanocomposite, Chem. Eng. J. 360 (2019) 423–434. https://doi.org/10.1016/j.cej.2018.11.231.

[89] K.H. Chu, Fixed bed sorption: Setting the record straight on the Bohart-Adams and Thomas models, J. Hazard. Mater. 177 (2010) 1006–1012. https://doi.org/10.1016/j.jhazmat.2010.01.019.

[90] W.J. Weber, J.C. Morris, Kinetics of Adsorption on Carbon from Solution, J. Sanit. Eng. Div. 89 (1963) 31–60.

[91] M.K. Shahid, S. Phearom, Y.G. Choi, Synthesis of magnetite from raw mill scale and its application for arsenate adsorption from contaminated water, Chemosphere. 203 (2018) 90–95. https://doi.org/10.1016/j.chemosphere.2018.03.150.

[92] A.T. Jacobson, M. Fan, Evaluation of natural goethite on the removal of arsenate and selenite from water, J. Environ. Sci. (China). 76 (2019) 133–141. https://doi.org/10.1016/j.jes.2018.04.016.